

# Interferometric Probing of Laser Generated Plasmas for Electron Acceleration

Diplomarbeit

FRIEDRICH-SCHILLER-UNIVERSITÄT JENA  
PHYSIKALISCH-ASTRONOMISCHE FAKULTÄT



eingereicht von Maria Reuter  
geboren am 17. Dezember 1985 in Jena

**Gutachter:**

1. Prof. Dr. Malte C. Kaluza
2. Prof. Dr. Gerhard G. Paulus

**Tag der Verleihung des Diploms:**

# Contents

|          |   |           |
|----------|---|-----------|
| <b>1</b> | <b>Introduction</b>   | <b>1</b>  |
| <b>2</b> | <b>Fundamentals</b>   | <b>3</b>  |
| 2.1      | Ultra Short Pulses . . . . .                                    | 3         |
| 2.1.1    | Mathematical Description . . . . .                              | 3         |
| 2.1.2    | Propagation in Dispersive Media . . . . .                       | 6         |
| 2.1.3    | Chirped Pulse Amplification (CPA) . . . . .                     | 7         |
| 2.1.4    | Single Shot Autocorrelation . . . . .                           | 8         |
| 2.2      | Laser-Plasma Interaction . . . . .                              | 10        |
| 2.2.1    | Plasma Generation . . . . .                                     | 11        |
| 2.2.2    | Electron Motion in Strong Electromagnetic Fields (2D) . . . . . | 12        |
| 2.2.3    | Plasma Parameters . . . . .                                     | 15        |
| 2.2.4    | Nonlinear Relativistic Effects . . . . .                        | 16        |
| 2.2.5    | Laser Wakefield Acceleration . . . . .                          | 19        |
| <b>3</b> | <b>Experimental Setup and Methods</b>                           | <b>22</b> |
| 3.1      | The JETI-Laser System . . . . .                                 | 23        |
| 3.2      | Electron Acceleration Setup and Diagnostics . . . . .           | 25        |
| 3.2.1    | Setup and Characterization of the Probe Beam . . . . .          | 26        |
| 3.2.2    | The Normarski Interferometer . . . . .                          | 37        |
| 3.2.3    | The Electron Spectrometer . . . . .                             | 38        |
| <b>4</b> | <b>Interferometric Plasma Probing</b>                           | <b>40</b> |
| 4.1      | Electron Density and Phase of the Probe Beam . . . . .          | 40        |
| 4.2      | Phase Measurement . . . . .                                     | 42        |
| 4.3      | Phase Retrieval . . . . .                                       | 43        |

## Contents

---

|          |  |           |
|----------|--|-----------|
| 4.3.1    | Removal of Disturbing Frequencies from the Interferogram via Fourier Filtering . . . . . | 43        |
| 4.3.2    | Phase Calculation . . . . .  | 45        |
| 4.4      | Abel inversion . . . . .   | 46        |
| 4.4.1    | General Idea . . . . .   | 46        |
| 4.4.2    | Discrete Abel Inversion . . . . .  | 47        |
| <b>5</b> | <b>Results</b>   | <b>49</b> |
| 5.1      | Evolution of the Plasma Density . . . . .  | 49        |
| 5.1.1    | Accuracy of Optical Plasma Probing . . . . .   | 55        |
| 5.2      | Pointing and Divergence of the Electron Beam . . . . .                                   | 66        |
| 5.3      | Electron Spectra . . . . .   | 67        |
| 5.4      | Correlations . . . . .   | 68        |
| <b>6</b> | <b>Summary</b>   | <b>72</b> |
|          | <b>Appendices</b>  | <b>II</b> |
|          | <b>Bibliography</b>  | <b>VI</b> |
|          | <b>Danksagung</b>  | <b>XI</b> |

# 1 Introduction

*Physics is like sex.*

*Sure, it may give some practical results, but that's not why we do it.*

**R. Feynman**

In fundamental research, particle accelerators are widely used to generate particle as well as electromagnetic radiation. For conventional accelerators, the electrical field strengths are limited to<sup>1</sup> 10-50 MeV/m due to their damage threshold. Thus, distances of at least 20 m are necessary to accelerate particles to energies in the GeV-range.

In 1979, Tajima and Dawson proposed an acceleration mechanism based on laser plasma interaction<sup>2</sup>. A plasma wave is excited by a laser pulse with an enormous intensity. Immense longitudinal electric fields<sup>1</sup> of 10-100 GV/m originate from the associated charge separation. In subsequent years, the acceleration process has been investigated via simulations. Pukhov and Meyer-ter-Vehn<sup>3</sup> predicted quasi monoenergetic electron bunches in a *highly non-linear broken-wave regime* in 2002. Two years later, these electron bunches have been generated experimentally<sup>4-6</sup>. Guiding a laser pulse in a capillary extends the dimension of the plasma in laser direction and thus, the interaction length, so that electron energies in the GeV-range can be reached within few centimeters<sup>1</sup>.

A thorough observation of the processes occurring during the acceleration is required in order to control the parameters of the generated particle radiation as accurately as possible. Interferometry and shadowgraphy using a short, synchronized optical probe pulse are expedient possibilities<sup>7</sup>. Thus, the temporal evolution of the acceleration process can be quantified.

In 2002, such a probe beam was built for the JETI-laser system of the Institute of Optics and Quantumelectronics in Jena<sup>8</sup>. However, due to the upgrade of the JETI-laser system in autumn 2009, the probe pulse had to meet new requirements. One of the motivations modifying the laser system was to shorten the pulses from 80 to sub-30 fs. With shorter laser pulses higher

intensities are feasible. Moreover, laser pulses with a duration of 30 fs are well-suited for electron acceleration in the wakefield of these pulses.

Decreasing the pulse duration requires a broader spectrum which is more susceptible to dispersion than a narrow one. For this reason, dispersive effects occurring within the setup of the probe beam have to be minimized. Furthermore, an option to measure the pulse duration should be available. In this case, the pulse can be compressed to its minimal pulse duration limited by higher order dispersion using dispersive mirrors.

In an experiment at the JETI-laser system, the electron density in the plasma has been probed and simultaneously, the electron energy has been measured. On this basis, the ideal parameters for laser wakefield acceleration could be determined. The present thesis is focused on setup, characterization and application of the new JETI-probe beam. In the second chapter important fundamentals concerning short laser pulses and laser-plasma interaction are discussed. Consecutively, the setup of an experiment employing the probe beam in the field of laser wakefield acceleration is introduced. Chapter four contains the analysis method used to evaluate the data obtained by means of the probe beam. Results and conclusions are presented in chapter five.

## 2 Fundamentals

Relativistic laser plasma interaction is feasible as soon as the laser intensity is sufficient to enhance a particles energy about its rest energy<sup>9</sup>. At a wavelength of 800 nm, the minimum required pulse intensity for electrons<sup>10</sup> amounts to  $2.14 \times 10^{18} \text{ W/cm}^2$ .

### 2.1 Ultra Short Pulses

In this section ultra short laser pulses are discussed. At the beginning, the mathematical description is given. After that, the propagation in dispersive media is explained. Finally, methods to amplify and measure the duration of ultra short laser pulses are introduced.

#### 2.1.1 Mathematical Description

Laser pulses propagating in  $z$ -direction can be described enclosing the fast oscillation of an electromagnetic field defined by its wave vector  $k$  and carrier angular frequency  $\omega$  with an envelope function  $\mathcal{E}_0(z, t)$  determining the pulse shape and duration (Figure 2.1).

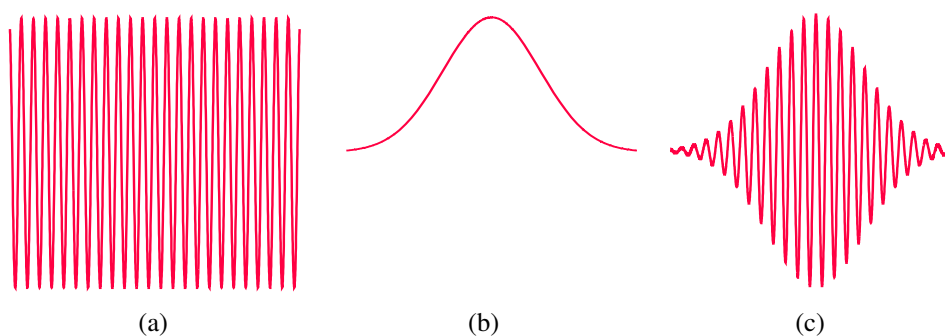


Figure 2.1: Multiplying a fast oscillation (a) with an envelope function (b) a short laser pulse (c) can be described. Pulse shape and duration depend on the spectral distribution and the phase of the single frequency components relative to each other.

Figure 2.1(c) is represented by<sup>11</sup>

$$\mathcal{E}(z, t) = \mathcal{E}_0(z, t) \cos(kz - \omega t). \quad (2.1)$$

Expressed as a complex function

$$\tilde{\mathcal{E}}(z, t) = \tilde{\mathcal{E}}_0(z, t) \exp\{i(kz - \omega t)\} + \text{c.c.} \quad (2.2)$$

it is related to the spectral distribution of the laser pulse via Fourier transformation

$$\tilde{\mathcal{E}}(z, t) = \frac{1}{2\pi} \int_{-\infty}^{\infty} \tilde{\mathcal{E}}(z, \omega) \exp\{i(kz - \omega t)\} d\omega \quad (2.3)$$

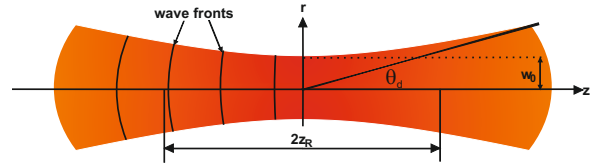
$$= \tilde{\mathcal{E}}_0(z, t) \exp\{i(kz - \omega t)\} \quad (2.4)$$

with a tilde attached to the symbols labeling complex functions and variables and c.c. denoting the complex conjugate.

### Gaussian Pulses

In the special case of a pulse with a transverse Gaussian intensity profile

$$I \propto \exp \left\{ -4 \ln 2 \left( \frac{r}{w(z)} \right)^2 \right\}, \quad (2.5)$$



the beam diameter is determined by twice its beam radius  $w$ . For a Gaussian beam propagating in  $z$ -direction (Figure 2.2) the beam radius<sup>12</sup> is given by

Figure 2.2: Gaussian beam with the Rayleigh length  $z_R$ , beam waist  $w_0$  and angle of divergence  $\theta_d$ .

$$w(z) = w_0 \left[ 1 + \left( \frac{z}{z_R} \right)^2 \right]^{\frac{1}{2}} \quad (2.6)$$

where  $w_0$  is the radius of the focus at the beam waist and  $z_R$ , its Rayleigh length given by



$$z_R = \frac{\pi w_0^2}{\lambda_L}. \quad (2.7)$$

Twice the Rayleigh length indicates the FWHM of the peak intensity in forward direction and therefore, defines the distance along which the pulse is considered to be focused. For  $z$  tending to infinity the ratio of  $w(z)$  and  $z$  is

$$\lim_{z \rightarrow \infty} \frac{w(z)}{z} = \lim_{z \rightarrow \infty} w_0 \sqrt{\frac{1}{z^2} + \frac{1}{z_R^2}} = \frac{w_0}{z_R}. \quad (2.8)$$

Calculating the inverse tangent of this ratio yields the natural diffraction

$$\theta_d = \arctan \frac{w_0}{z_R} \quad (2.9)$$

of the beam leading to defocusing.

To define a pulse duration  $\tau$ , the full width at half maximum (FWHM) of the pulse intensity is an adequate and easily accessible quantity. For a pulse with a longitudinal Gaussian intensity profile

$$I(t) \propto \exp \left\{ -4 \ln 2 \left( \frac{t}{\tau_{\text{FWHM}}} \right)^2 \right\}, \quad (2.10)$$

the transform limited pulse duration, i.e., the shortest possible pulse duration for a given spectrum, can be stated as<sup>12</sup>

$$\tau_{\text{FWHM}} = \frac{0.44}{\Delta\omega_{\text{FWHM}}}. \quad (2.11)$$

However, for a pulse affected by dispersion this equation does not hold. The more dispersion a pulse experiences the longer the pulse.

### 2.1.2 Propagation in Dispersive Media

A pulse is transform limited, if its spectral components are in the same phase. However, in a medium exhibiting a frequency dependent refractive index  $\eta(\omega)$ , single frequency components propagate at different velocities. In normal dispersive media, the shorter wavelength components are delayed with respect to the higher ones. Vice versa, the medium is called anomalous dispersive. Hence, the broader the spectrum of a pulse and therefore, the shorter the transform limited pulse duration, the more strongly the pulse shape and, as a consequence, duration is affected by dispersion.

The dispersion relation<sup>13</sup>

$$k(\omega) = \frac{\omega}{c}\eta(\omega) \quad (2.12)$$

can be derived from the wave equation applying Fourier transformation. Inserting this into the phase of an electromagnetic wave

$$\phi(\omega) = kz - \omega t \quad (2.13)$$

gives

$$\phi(\omega) = \frac{\omega}{c}\eta(\omega)z - \omega t. \quad (2.14)$$

Expressing the electric field in terms of the phase<sup>11</sup>

$$\tilde{\mathcal{E}}(z, \omega) = \tilde{\mathcal{E}}(0, \omega)\exp[-i\phi(\omega)], \quad (2.15)$$

and Tailor expanding the phase with respect to the central angular frequency  $\omega_0$

$$\phi(\omega) = \phi(\omega_0) + \sum_{n=1}^{\infty} \frac{1}{n!}\phi^{(n)}(\omega_0)(\omega - \omega_0)^n \quad (2.16)$$

the influence of the single terms on the temporal behavior of a pulse can be investigated.

- $\phi_0 = \phi(\omega_0) = k(\omega_0)z$  is the time independent absolute phase of an electromagnetic wave in vacuum as well as in dispersive media. Higher orders of the angular frequency are only affected by dispersive media.

- $\phi^{(1)}(\omega_0) = \partial\phi_0/\partial\omega$  causes a temporal shift of the pulse as an entity.
- $\phi^{(2)}(\omega_0) = \partial^2\phi_0/\partial\omega^2$  represents the group delay dispersion (GDD). The duration of a pulse experiencing GDD is linearly increased by a factor  $\text{GDD} \times \Delta L$  with  $\Delta L$  representing the length of the dispersive medium.
- $\phi^{(3)}(\omega_0) = \partial^3\phi_0/\partial\omega^3$  is called third order dispersion (TOD) and leads to asymmetrical pulse shapes or even pre and post pulses.

### 2.1.3 Chirped Pulse Amplification (CPA)

Relativistic laser plasma interaction requires the pulse energy to be amplified. The pulse intensity

$$I = \frac{E}{\tau A} \quad (2.17)$$

is dependent on the pulse energy  $E$ , the pulse duration  $\tau$  and the beam area  $A$ , i.e, the intensity increases due to amplification if  $\tau$  and  $A$  are kept constant. Nevertheless, the intensity must not exceed the damage threshold of the optical components. The active medium used in the JETI-laser system (section 3.1), titanium doped sapphire (Ti : Sa), is damaged when it is exposed to intensities  $\gtrsim 10^{10} \text{ W/cm}^2$ . To keep the peak intensity underneath this value, the pulse duration and the area can be adjusted to an appropriate value before the pulse energy is increased. With an expansion telescope, the area can be increased easily. In spite of that, the spot size is limited by the apertures of the components available and the focal length of the final focusing optic. Furthermore, large optical components are expensive, difficult to handle and require a lot of space.

For this reason, one takes advantage of pulse stretching via linear dispersion<sup>14</sup>. The short pulse propagates through a stretcher which imprints a reversible group velocity dispersion on the pulse. The laser pulse exiting the stretcher has a varying instantaneous frequency and is called a chirped pulse. Owing to its longer duration a chirped pulse has a lower peak intensity. Unchirping the pulse in a compressor, high peak powers can be reached. A possible setup for a stretcher and a compressor, respectively, is introduced in section 3.1. The principle of chirped pulse amplification is visualized in Figure 2.3.

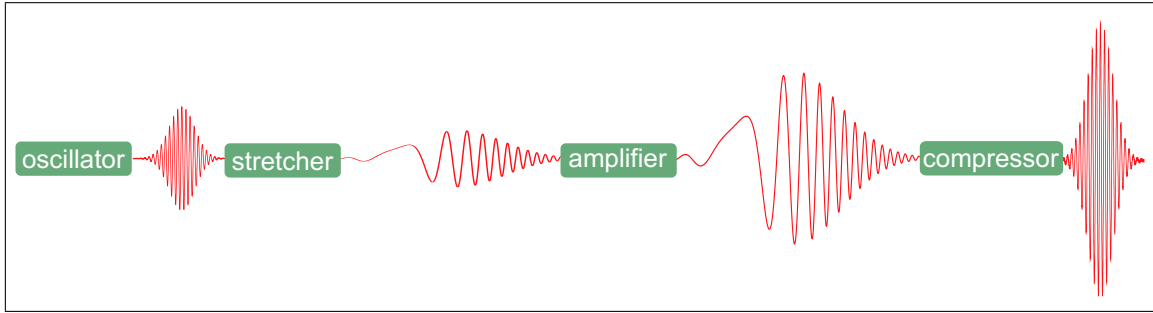


Figure 2.3: A short pulse is stretched delaying its spectral components with respect to each other, i.e., the instantaneous frequency changes within the pulse. After amplification, the duration of the long high-energy pulse is reduced almost to its initial value in the compressor. This scheme is adapted from reference<sup>15</sup>.

### 2.1.4 Single Shot Autocorrelation

“In order to measure an event in time, you must use a shorter one. But then, to measure the shorter event, you must use an even shorter one. And so on. So, now, how do you measure the shortest event ever created?”<sup>16</sup>.

With the technique of intensity autocorrelation it is possible to avoid this *dilemma*. Splitting a pulse into two replica and delaying them relative to each other creates a gate which is shorter than the pulse. The width of the gate function depends on the temporal delay between the two pulses<sup>11</sup>.

### Nonlinear Optics

For laser pulses with an intensity exceeding  $10^9 \text{ W/cm}^2$ , the relation between electric field  $\vec{E}(\vec{r}, \omega)$  and the polarization  $\vec{P}(\vec{r}, \omega)$  cannot be approximated by its linear term  $\vec{P} = \epsilon_0 \chi^{(1)} \vec{E}$  anymore. Instead, the polarization has to be developed in a power series with respect to the electric field<sup>17</sup>

$$\vec{P} = \epsilon_0 [\chi^{(1)} \vec{E} + \chi^{(2)} \vec{E} \vec{E} + \chi^{(3)} \vec{E} \vec{E} \vec{E} + \dots] \quad (2.18)$$

$$= \epsilon_0 \chi \vec{E} \quad (2.19)$$

where  $\epsilon_0$  denotes the vacuum permittivity and  $\chi$  the effective nonlinear susceptibility. In a crystal exhibiting a second order susceptibility  $\chi^{(2)}$ , the frequency of an incident signal can be

doubled. This process is called second harmonic generation (SHG).

### Principle of Single Shot Autocorrelation

Two replica of one pulse are superimposed inside a nonlinear crystal at an angle<sup>18;19</sup> (section 3.2.1). Inside this nonlinear crystal the second harmonic of the incident signal is generated. As the spatial width of the second harmonic depends on the angle between the two pulses and their duration<sup>20</sup>, the spatial information can be transformed into a temporal one.

A calibration factor  $f_c$  translating a number of pixels of a CCD chip into a value of time is needed to retrieve the pulse duration from the image of the second harmonic. The width of the second harmonic  $w_{\text{SHG}}$  and therefore, the calibration factor, depends on the angle at which the two pulses are superimposed inside the crystal (Figure 2.4), i.e., as long as the angle between the pulses is kept constant, the calibration factor does not change.

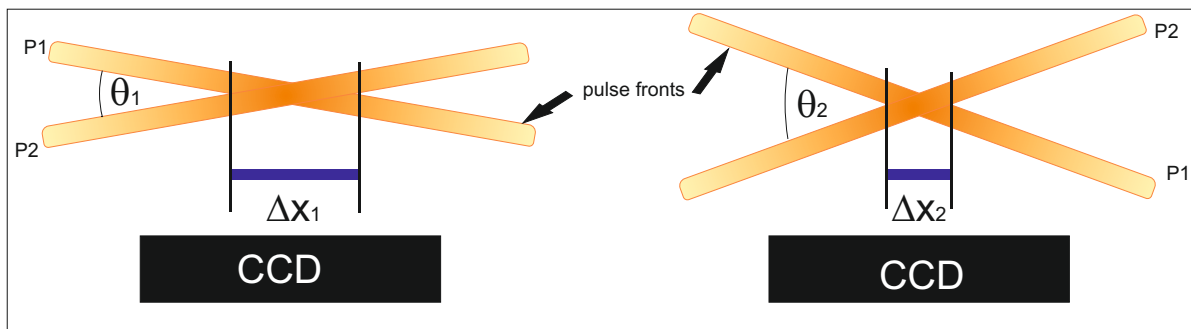


Figure 2.4: The angle between the pulses determines the calibration factor: the larger the angle between the pulses the smaller the width of the signal and thus, the smaller the calibration factor.

When the two pulses are delayed with respect to each other, the x-position at which the two pulses are superimposed inside the crystal changes (Figure 2.5), i.e., the second harmonic moves across the crystal and can then be imaged onto a CCD chip.

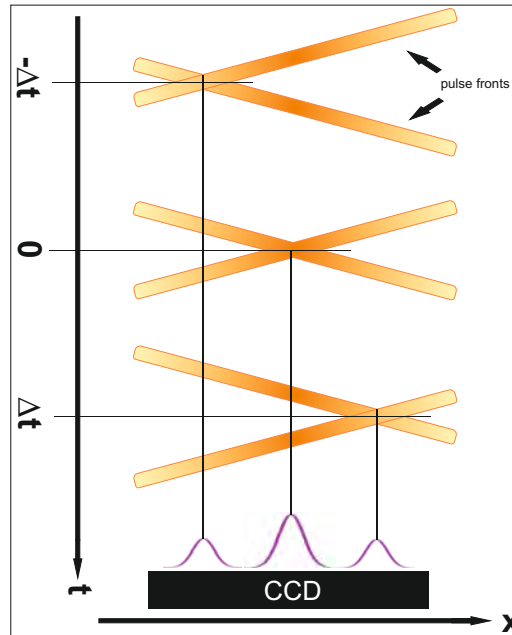


Figure 2.5: Changing the delay between the two pulses causes a shift of the signal at the CCD camera. Relating this shift to the corresponding displacement of the translation stage and therefore, to the temporal shift of the pulses, yields the calibration factor.

The  $x$ -position of the maximal intensity of the signal is linearly related to the relative delay between the two pulses. The slope of this line is the calibration factor in units of time per pixel. Additionally, a scaling factor  $f_s$  is needed to account for the pulse shape. It is  $1/\sqrt{2}$  for Gaussian pulses<sup>11</sup>. The pulse duration  $\tau$  can be calculated with

$$\tau = f_c f_s w_{\text{SHG}}. \quad (2.20)$$

## 2.2 Laser-Plasma Interaction

In this section, the application of highly intense laser pulses in the field of plasma physics is explained. Consecutively, plasma generation, mutual influence of laser pulse and plasma as well as electron motion in a laser field and their acceleration in the wakefield of the laser pulse are elucidated.

### 2.2.1 Plasma Generation

To ionize a substance, its ionization energy  $E_{\text{ion}}$  has to be applied. Via the photoelectric effect, free electrons are generated if the angular frequency  $\omega$  of the incident radiation is sufficient so that  $E_{\text{ph}} = \hbar\omega \geq E_{\text{ion}}$  holds. The energy to singly ionize helium<sup>21</sup> amounts to 24.6 eV. Therefore, a titanium sapphire laser with a photon energy of about 1.55 eV cannot ionize helium by means of the photoelectric effect.

Nevertheless, it is possible to ionize a medium although the photon energy  $E_{\text{ph}}$  is smaller than  $E_{\text{ion}}$ . When the light intensity  $I$  and therefore, the photon flux, is sufficient, more than one photon can be absorbed contemporaneously. Ionization takes place if  $nE_{\text{ph}} \geq E_{\text{ion}}$ , where  $n$  is the number of photons absorbed simultaneously. This process is referred to as multi photon ionization (MPI).

Further increasing the intensity, the Coulomb potential of the atoms or molecules is transformed into a potential barrier. With a certain probability, the electrons then can tunnel through this barrier. In dependence on the ionization potential of the substance and the intensity of the radiation it can be estimated which ionization mechanism takes place with the Keldysh parameter<sup>22</sup>

$$\Gamma = \sqrt{\frac{E_{\text{ion}}}{2\phi_{\text{pond}}}}. \quad (2.21)$$

The ponderomotive potential  $\phi_{\text{pond}}$  depends on the ponderomotive force which is introduced in section 2.2.2. A Keldysh parameter smaller than one indicates tunnel ionization and vice versa if  $\Gamma \gtrsim 1$ , multi photon ionization takes place.

For light intensities exceeding<sup>23</sup>  $4 \times 10^9 (E_{\text{ion}}/\text{eV})^4 Z^{-2} \text{W}/\text{cm}^2$ , over the barrier ionization (OBI) is the dominating ionization mechanism: the Coulomb potential is modified by the electric field of the laser pulse to such an extent that electrons can leave the atom at two instances during one laser period (Figure 2.6) and a plasma with an initial electron density  $n_{e0}$  is generated. The electron density depends on the gas density and on the laser intensity. The higher the gas density and the laser intensity the higher the electron density. For MPI and tunnel ionization the electron density is lower than for OBI as the atoms or molecules are ionized with a probability smaller than one.

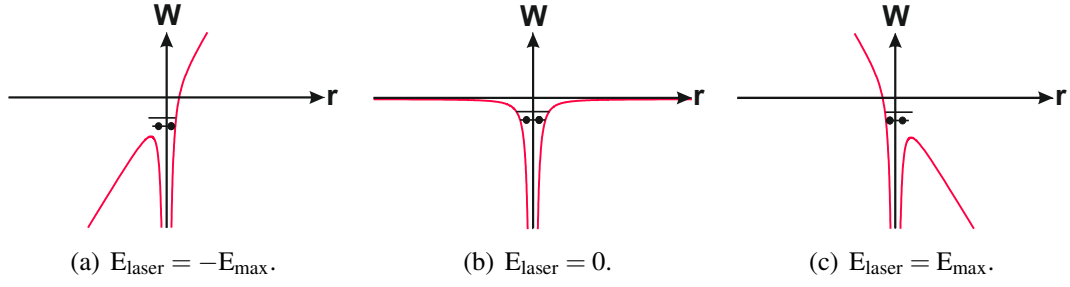


Figure 2.6: In dependence on the electric field of the laser pulse, the Coulomb potential of the atom (b) can be disturbed. If the laser field is sufficient, the Coulomb barrier is suppressed (a), (c).

Helium has ionization energies<sup>21</sup> of 24.6 eV and 54.4 eV for single or double ionization, respectively. With an atomic number of  $Z=2$ , the intensity threshold to singly ionize it is  $1.4 \times 10^{15}$  while  $8.8 \times 10^{15}$  W/cm<sup>2</sup> is sufficient for full ionization<sup>23</sup>. As relativistic laser plasma interaction at least requires intensities in the range of  $10^{18}$  W/cm<sup>2</sup>, a fully ionized gas can be assumed.

## 2.2.2 Electron Motion in Strong Electromagnetic Fields (2D)

A plane wave propagating in z-direction can be described by its electric field

$$\vec{\mathcal{E}}(z, t) = \tilde{\mathcal{E}}_0(z, t) e^{i(kz - \omega t)} \vec{e}_x. \quad (2.22)$$

Calculating the magnetic field  $\vec{\mathcal{B}}$  by means of  $\nabla \times \vec{\mathcal{E}} = -\partial \vec{\mathcal{B}} / \partial t$  the it is given by

$$\vec{\mathcal{B}}(z, t) = \tilde{\mathcal{B}}_0(z, t) e^{i(kz - \omega t)} \vec{e}_y. \quad (2.23)$$

with  $\tilde{\mathcal{B}}_0 = \tilde{\mathcal{E}}_0 / c$  in vacuum.

For an electron with the elementary charge  $-e$  the total temporal derivative of the electrons momentum  $\vec{p}_e$

$$\frac{d\vec{p}_e}{dt} = -e(\vec{\mathcal{E}}(z, t) + \vec{v}_e \times \vec{\mathcal{B}}(z, t)) \quad (2.24)$$

is dependent on the electron velocity  $\vec{v}_e$ . Nevertheless, in the classical case, i.e., the electron has a velocity much smaller than the speed of light  $c$ , the fraction of force exerted to the electron by the  $\vec{\mathcal{B}}$ -field can be neglected. Thus, the solution of the equation of motion



is an oscillation induced by the alternating  $\vec{\mathcal{E}}$ -field. An electron oscillates transverse to the propagation direction of the electromagnetic wave with a maximum velocity

$$v_{\max} = \frac{e\mathcal{E}_0}{\omega_L m_e}. \quad (2.25)$$

When the maximum velocity of the electron is close to the speed of light, the classical description is no longer valid. Dividing equation 2.25 by  $c$  leads to a new quantity<sup>24</sup>

$$\frac{v_{\max}}{c} = \frac{e\mathcal{E}_0}{\omega_L m_e c} = a_0 \quad (2.26)$$

where  $a_0$  is the normalized amplitude of the vector potential of the electromagnetic wave which is connected to the laser intensity by

$$a_0 = \sqrt{\frac{I_L}{1.37 \times 10^{18} \text{ W/cm}^2} \frac{\lambda_L^2}{\mu\text{m}^2}}. \quad (2.27)$$

To reach  $a_0 \geq 1$  indicating the relativistic regime of electron motion and assuming a laser wavelength of  $\lambda_L = 0.8 \mu\text{m}$ , the laser intensity has to exceed  $I_L = 2 \times 10^{18} \text{ W/cm}^2$ .

In the relativistic case, the force originating from the  $\mathcal{B}$ -field cannot be omitted anymore and the electron experiences not only a transverse but also a longitudinal momentum. This longitudinal momentum causes a drift in laser direction superimposed with a oscillation with twice the frequency of the laser pulse. The drift velocity<sup>25</sup> can be stated as

$$v_{\text{drift}} = c \frac{a_0^2}{a_0^2 + 4}. \quad (2.28)$$

Perpendicular to the laser direction, the electron oscillates with the laser frequency. In a frame of reference moving with  $v_{\text{drift}}$  the electron carries out a figure-eight motion (Figure 2.7).

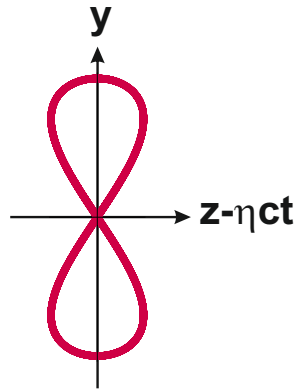


Figure 2.7: In the co-moving frame of reference the electron carries out a figure-eight motion.

The trajectory of an electron in the laboratory frame in a plane electromagnetic wave and a laser pulse, respectively, is illustrated in Figure 2.8. A plane electromagnetic wave drives an oscillation with equal expelling and restoring forces. Thus, the electron moves around its position of rest drifting with the velocity  $v_{\text{drift}}$ . For an electromagnetic wave with transverse and longitudinal intensity gradients, e.g., a focused laser pulse with a Gaussian intensity distribution, the alternating fields are not uniform anymore and the expelling forces exceed the restoring forces when the electron initially starts on axis.

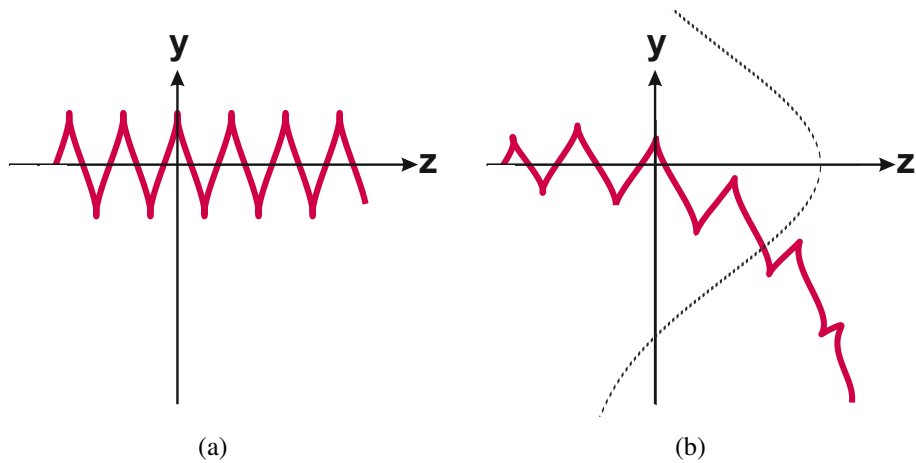


Figure 2.8: The trajectory of an electron in the laboratory frame in relativistic electromagnetic waves is depicted for (a) a plane wave and (b) a pulse with longitudinal and transverse intensity gradients. The black dashed line represents the transverse intensity profile of the laser pulse.

The resulting force averaged over one laser period is called *ponderomotive force*<sup>24</sup> which is

dependent on the gradient of the laser intensity

$$\vec{F}_{\text{pond}} = -\frac{e^2}{4 \langle \gamma \rangle m_e \omega_L^2} \vec{\nabla} I_L \quad (2.29)$$

In this equation the relativistic mass increase is accounted for by the averaged relativistic  $\gamma$ -factor

$$\langle \gamma \rangle = 1 + \frac{a_0^2}{4} \quad (2.30)$$

which increases with increasing normalized vector potential and thus, with increasing intensity.

### 2.2.3 Plasma Parameters

The ponderomotive force pushes electrons into regions of lower laser intensities. At intensities lower than  $10^{24} \text{ W/cm}^2$  the electron motion is affected by the laser field, while usually, the ions can be treated as a positively charged immobile background owing to their inertia. Expelling electrons from regions of high intensity leads to an electron density modulation causing longitudinal electric fields and electron density oscillations due to the quasi-static ion background. The oscillation frequency, referred to as plasma frequency, can be calculated by means of<sup>26;27</sup>

$$\omega_p = \sqrt{\frac{n_{e0} e^2}{\epsilon_0 m_e}}. \quad (2.31)$$

As the plasma wave is driven by the laser, the phase velocity of the plasma wave  $v_{\text{ph}_p}$  is equal to the group velocity of the laser  $v_{\text{gr}_L}$ .

If the plasma frequency is higher than the laser frequency  $\omega_L$ , the refractive index of the plasma<sup>26;27</sup>  $\eta = \sqrt{1 - n_e / (\langle \gamma \rangle n_{\text{cr}})} = \sqrt{1 - \omega_p^2 / (\langle \gamma \rangle \omega_L^2)}$  becomes imaginary and the laser pulse cannot propagate inside the plasma. Thus, above a critical electron density<sup>26;27</sup>, where the plasma frequency equals the laser frequency,

$$n_{\text{cr}} = \frac{\omega_L^2 \epsilon_0 m_e}{e^2} \quad (2.32)$$

the laser pulse is reflected by the plasma.

### 2.2.4 Nonlinear Relativistic Effects

While laser pulse and plasma are interacting, laser and plasma parameters influence each other mutually which considerably affects the acceleration process. Nonlinear effects and therefore, the laser intensity, influence the refractive index  $\eta$  which can be described for a plasma as<sup>25</sup>

$$\eta = \sqrt{1 - \frac{\omega_p^2}{\langle \gamma \rangle \omega_L^2}} = \sqrt{1 - \frac{n_e}{\langle \gamma \rangle n_{cr}}}. \quad (2.33)$$

The transverse intensity distribution of the laser pulse affects the ponderomotive force and the averaged relativistic  $\gamma$ -factor. Electrons are expelled from the laser axis and simultaneously, the radially decreasing averaged relativistic  $\gamma$ -factor causes a higher relativistic mass increase on laser axis. The interplay of electron number and mass results in a radially decreasing index of refraction. In consequence, the further the pulse propagates through the plasma the more its phase front is bent (Figure 2.9).

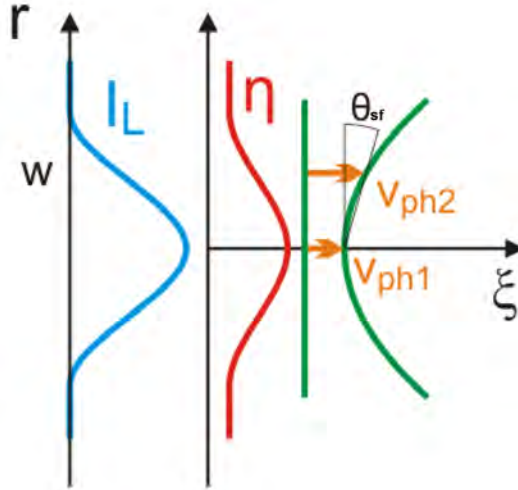


Figure 2.9: The transverse intensity distribution of the laser pulse (blue) causes ponderomotive forces as well as a radially decreasing averaged relativistic  $\gamma$ -factor. From that, a radially decreasing index of refraction (red) originates. Therefore, the phase velocity of the laser pulse increases radially so that the phase front of the laser pulse is bent. If the bending angle  $\theta_{sf}$  is sufficient to compensate the natural diffraction of the pulse, it is self focused. (Image courtesy of C. Widmann<sup>28</sup>)

The angle of **self focusing**  $\theta_{\text{sf}}$  can be calculated with<sup>25</sup>

$$\theta_{\text{sf}} = -\frac{c}{\eta^2} \frac{\partial \eta}{\partial r} \Delta t \quad (2.34)$$

If the bending angle  $\theta_{\text{sf}}$  is sufficient to compensate the angle of divergence  $\theta_{\text{d}}$ , a laser pulse is self focused, i.e. it is guided inside the plasma over a longer distance than the Rayleigh length  $z_{\text{R}}$  (see also section 2.1).

Longitudinally, the electron density of the plasma wave modulates the refractive index which influences the laser frequency and hence, the pulse duration. Depending on the electron density inside a medium and thus, on its refractive index, different parts of the pulse can experience frequency up or down shifts.

In a plasma wave, the front of a short pulse obeying  $c\tau_{\text{L}} \approx \lambda_{\text{p}}$  (Figure 2.11(a)) is exposed to a decreasing index of refraction and thus, is redshifted and steepens. In contrast, the back of the pulse experiences an increasing electron density, is therefore blueshifted and catches up with the lower frequencies. For this reason this process is referred to as **photon acceleration**<sup>29</sup>. In the co-propagating frame of reference expressed by  $\xi = z - ct$  the shift of the spectral components is given by<sup>24</sup>

$$\frac{1}{\omega_{\text{L}}} \frac{\partial \omega_{\text{L}}}{\partial t} = \frac{c}{\eta^2} \frac{\partial \eta}{\partial \xi}. \quad (2.35)$$

In the spatial domain, the spectral components approach each other spatially resulting in **pulse compression** (Figure 2.11(c)), i.e. the pulse duration is shortened. The influence of the refractive index on phase and group velocity of the laser, causing photon acceleration and pulse compression, respectively, is illustrated in Figure 2.10.

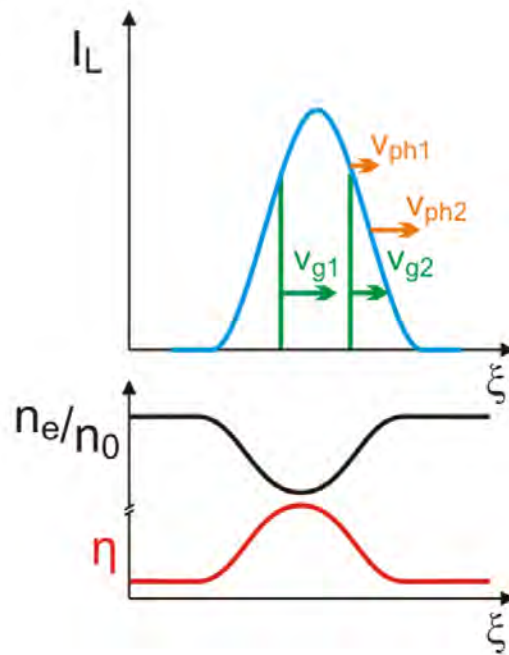


Figure 2.10: The red line represents the refractive index corresponding to the normalized electron density within one period of the plasma wave (black line). If the laser pulse (blue) obeys  $c\tau_L \approx \lambda_p$ , its front experiences a decreasing refractive index while its back is exposed to an increasing one. Phase (orange) and group velocity (green) are affected by the gradient of the refractive index. In the Fourier domain one speaks of photon acceleration and in the spatial domain of pulse compression. (Image courtesy of C. Widmann<sup>28</sup>)

In the case of a long pulse (Figure 2.11(b)) with  $c\tau_L \gg \lambda_p$ , the pulse is split in several pulselets (Figure 2.11(d)) as each part of a pulse situated in a distinct period of the plasma wave is compressed separately.

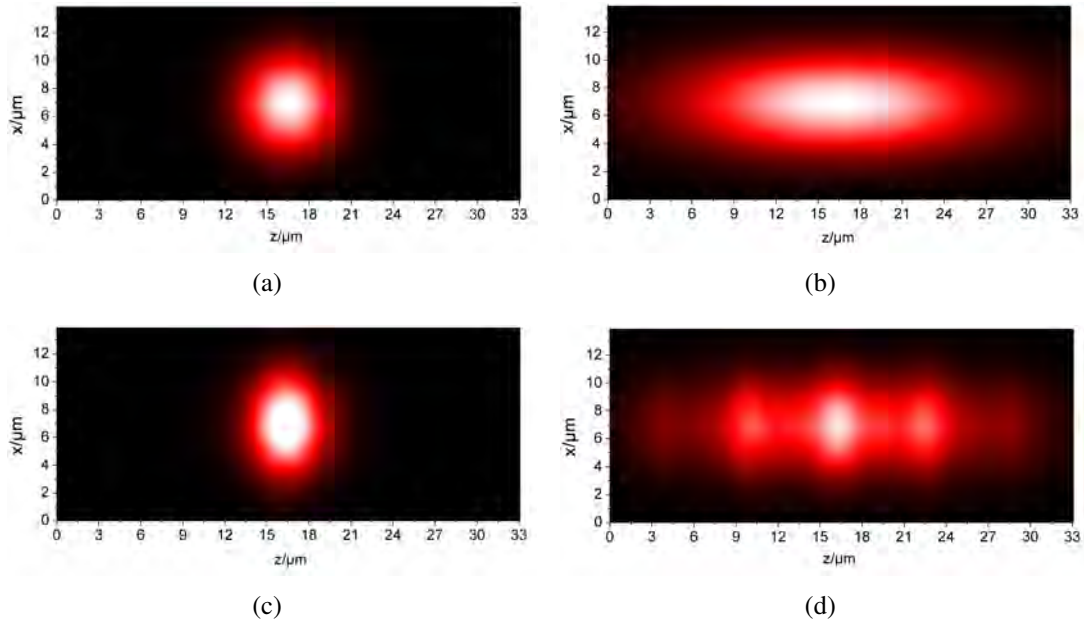


Figure 2.11: Four pulses propagating in  $z$ -direction are illustrated. (a) and (b) propagate in vacuum, (c) and (d) are modulated in a plasma wave with a wavelength of  $6\ \mu\text{m}$ . A short pulse (a) with a duration in the range of the plasma wavelength is compressed within one period of the plasma wave (c) while a long pulse whose duration strongly exceeds one period of the wave (b) is split (d) as each pulselet is compressed in a separate period of the plasma wave.

## 2.2.5 Laser Wakefield Acceleration

### Acceleration in One Dimension

The longitudinal electric field generated by the electron density oscillation can be used to efficiently accelerate electrons if they are injected into the minimum of the electric field  $\mathcal{E}_{\text{acc}}$  pointing against the laser direction. Injecting electrons externally requires an accuracy of at least  $\lambda_p/2$  which is in the order of few  $\mu\text{m}$ . This can be avoided by driving the plasma wave so hard that single electrons become faster than the phase of the plasma wave leading to *wave breaking*, i.e., electrons are self-injected from the maximum of electron density into the accelerating longitudinal electric field by the plasma wave. Wave breaking occurs when the electric field generated by the plasma wave exceeds the threshold field strength that can be

derived as<sup>30</sup>

$$\mathcal{E}_{\text{th}} = \frac{m_e c \omega_p}{e} \sqrt{2(\gamma - 1)}. \quad (2.36)$$

The the regions where the electric field can accelerate electrons in forward direction move along the laser axis with the phase velocity of the plasma wave  $v_{\text{php}}$ . The electrons propagating faster than the phase of the wave are bound to run out of the accelerating region as the longitudinal electric field changes its orientation at the minimum of the electron density. From this point on electrons are decelerated, i.e. the *dephasing limit* is reached. The distance over which electrons can be accelerated in a plasma wave is called *dephasing length*  $d_{\text{dl}}$  and can be calculated with<sup>24</sup>

$$d_{\text{dl}} = \lambda_p \left( \frac{\omega_L}{\omega_p} \right)^2 = \lambda_p \left( \frac{n_{\text{cr}}}{n_e} \right) \quad (2.37)$$

in the laboratory frame. The higher the electron density, the shorter the dephasing length. If the dephasing limit is reached when the accelerated electrons reach the boundary of the plasma, deceleration of the electrons can be avoided and the electrons exhibit maximal energy. Assuming the accelerating field is constant all over the acceleration length, the maximal energy is given by<sup>2</sup>

$$E_{\text{max}} = e \int_0^{d_{\text{dl}}} \mathcal{E}_{\text{acc}} dz = \frac{\pi}{2} m_e c^2 a_0^2 \frac{n_{\text{cr}}}{n_e} \quad (2.38)$$

Nevertheless, with certain distributions of the electron density, the dephasing limit can be overcome partially<sup>31</sup>. Furthermore, the electron energy and the stability of the process can be increased by controlled injection<sup>32;33</sup>.

### Acceleration in Three Dimensions

As electrons are expelled from the laser axis in each direction the resulting three dimensional plasma wave can be comprehended as a pulsating electron density distribution. At the back of the laser pulse, a region of low electron density is generated by the ponderomotive force. In the highly non-linear broken-wave regime<sup>3</sup> this region is completely free of electrons and a



so-called bubble is formed. Electrons at the edge of the bubble move against the laser direction to the end of the bubble where a fraction of these electrons can be injected into the accelerating electric field. Due to the curvature of the bubble, the generated electric field has a focusing effect on the electrons. While electrons injected on the axis of symmetry are accelerated longitudinally, electrons injected off-axis additionally have a transverse velocity component causing a divergent electron bunch. Figure 2.12 illustrates the principle of laser wakefield acceleration in the bubble regime.

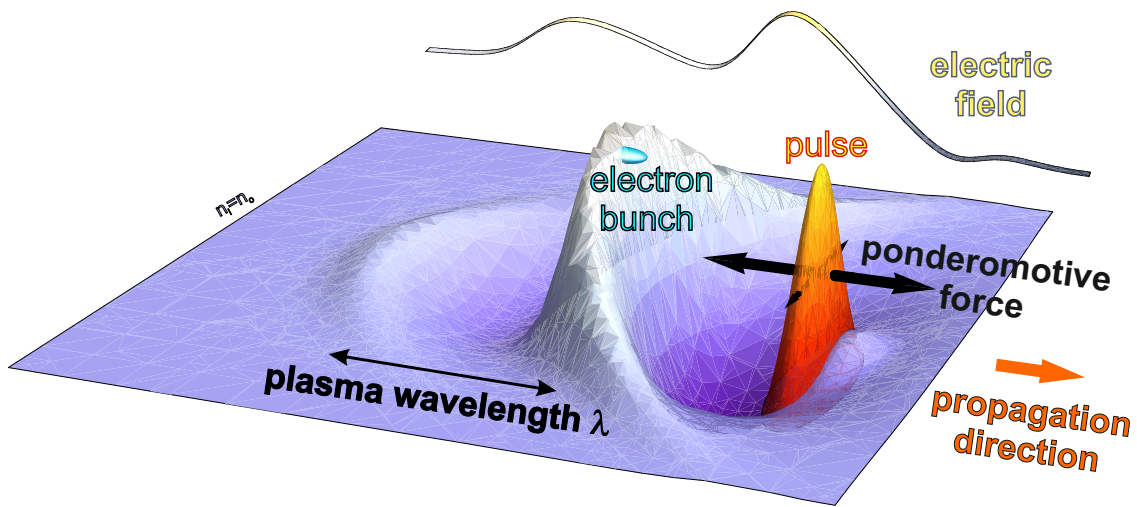


Figure 2.12: Along its way through the gas jet, the front of the laser pulse (orange) ionizes the atoms. Due to the ponderomotive force of the laser pulse (black arrows), the electrons are expelled from the regions of the highest laser intensities. Restoring forces and inertia cause a plasma wave (violet), i.e., the electrons oscillate with respect to the positive ion background. If the intensity of the laser pulse is sufficient, the region behind the laser pulse is free of electrons. When the generated plasma wave breaks and electrons (cyan) are injected into the longitudinal electric field (grey/yellow), the electrons are accelerated highly efficiently. The electric field is calculated using Poisson's equation.

### 3 Experimental Setup and Methods

In order to accelerate electrons to relativistic velocities with a laser pulse, a system generating these pulses with intensities in the range of  $10^{18} \text{ W/cm}^2$  and a target providing the electrons is required. In this chapter, the JETI-laser system of the Institute of Optics and Quantumelectronics in Jena as well as the setup of an experiment in the field of laser wake field acceleration is introduced. However, the focus of this chapter is on the setup of the probe beam.

To provide a simple overview, Figure 3.1 depicts the schematic arrangement of the laser system together with the target chamber and the probe beam. Both, the laser system and the experimental setup are illustrated and explained in the following in more detail.

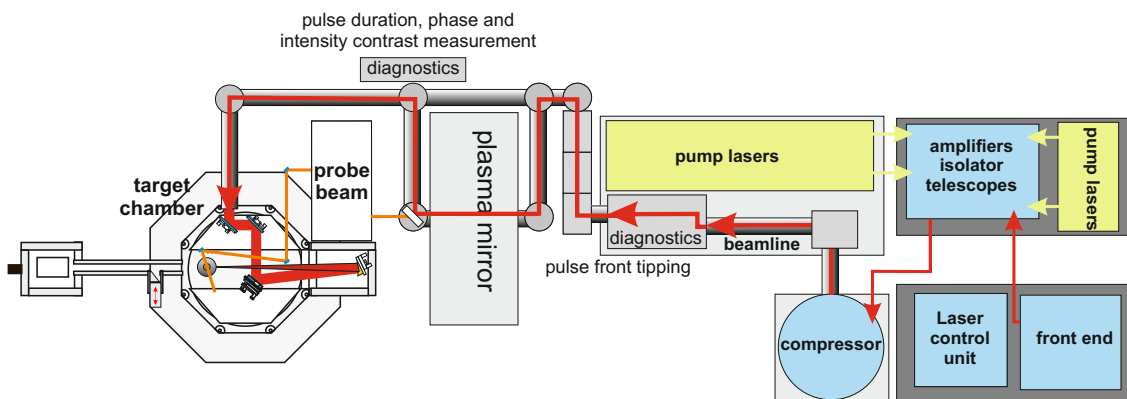


Figure 3.1: Scheme of the laser system (right hand side) and setup of an experiment on electron acceleration including the target chamber and the probe beam. Starting at the vacuum compressor, the beam line is evacuated. The probe beam (orange) is split from the main beam (red) after the plasma mirror chamber where 1% is transmitted through a dielectric beam splitter.

### 3.1 The JETI-Laser System

In this section, the setup of the JETI-laser system upgraded in 2009 is described. Owing to the broader spectrum, shorter laser pulses are available. The previous setup of the laser system is described in a number of publications, e.g.<sup>34</sup>. For this reason, most importance is attached to recent modifications. The main components are illustrated schematically in Figure 3.2. Employing the CPA principle (section 2.1.3), with the JETI-laser system pulses of about 800 mJ and a duration of 27 fs can be generated. Within the whole system, titanium doped sapphire is used as active medium pumped by frequency doubled Nd : YAG-lasers.

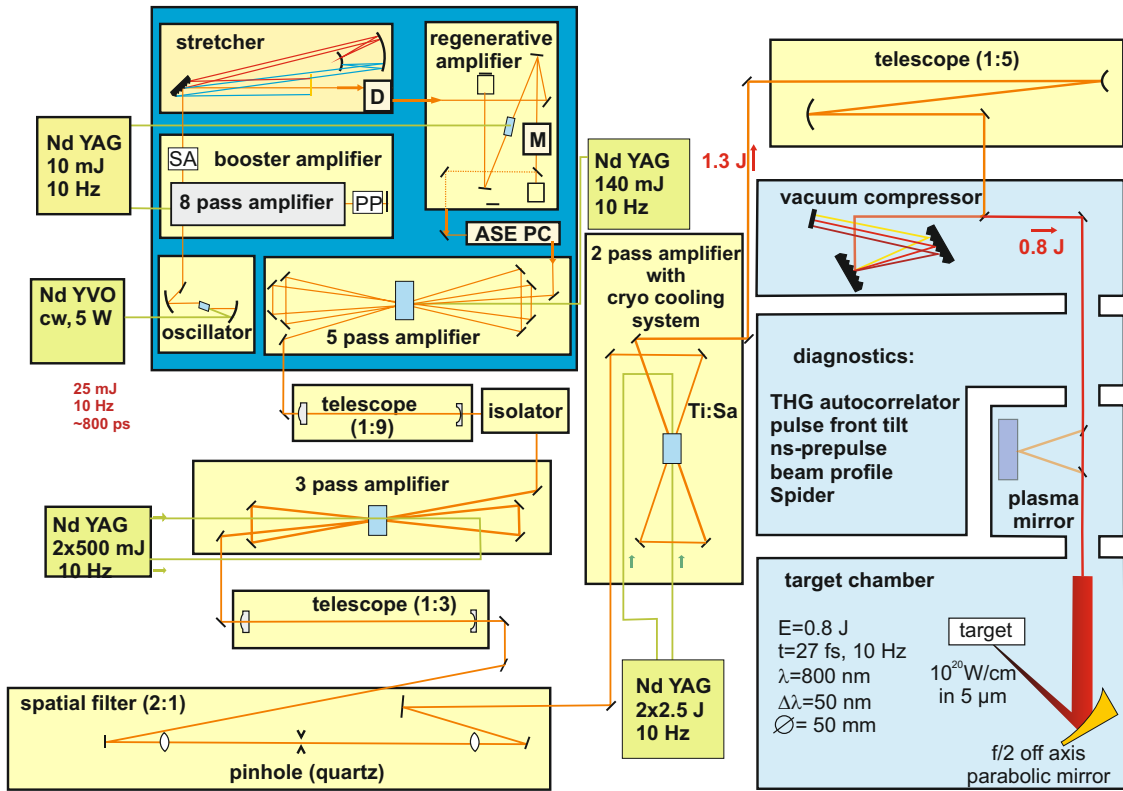


Figure 3.2: Schematic setup of the JETI-laser system.

In the mode locked oscillator, pulses with a bandwidth of 74 nm and a center wavelength of 805 nm are generated at a repetition rate of 76 MHz. These pulses enter the booster module where the YAG pulse energy is enhanced in an 8-pass amplifier. A pulse picker (PP) reduces the repetition rate to 10 Hz before the pulses are coupled into the 8-pass amplifier for the second time. With the grating stretcher, the pulse duration is stretched to about 800 ps. Included into

the stretcher box, an acousto-optic programmable dispersive filter (D) compensates higher order dispersion induced by the stretcher or optical components further down the laser chain. Hence, sub-30 fs pulses are feasible. In the regenerative amplifier, the pulses are kept until amplification saturation is reached at approximately 1 mJ. Every time the pulses have passed the active medium inside the regenerative amplifier, an acousto-optic programmable gain control dispersive filter (M) minimizes the effect of gain narrowing in the amplifiers attenuating the intensity at the central frequencies. Afterwards, an ASE Pockels cell eliminates ns-prepulses before the pulses enter the 5-pass amplifier. Leaving the front end, the pulses have an energy of 25 mJ.

Except the vacuum compressor, the following components do not have been modified significantly during the upgrade. A Faraday isolator prevents the front end from radiation backscattered from the subsequent amplifiers or the target and the laser pulse energy is increased to 300 mJ in the consecutive 3-pass amplifier. Afterwards, the laser mode is cleaned using a spatial filter. Finally, in the 2-pass amplifier with a cryogenic cooling system, the laser pulses are amplified to 1.3 J. The vacuum compressor compresses the pulse duration to about 27 fs. After the compressor a pulse energy of 800 mJ is available owing to its efficiency. For intensities exceeding  $10^{13}$  W/cm<sup>2</sup> effects like self focusing, ionization and dispersion disturb the beam profile when the laser pulses propagate through material such as glass or even air. Therefore, the pulses are guided inside a vacuum system. A plasma mirror<sup>36</sup> can be used to increase the intensity contrast of the pulses by three orders of magnitude. The smaller the ratio of the intensity of potential pre pulses to the peak intensity of the main pulse the higher the intensity contrast. For further enhancement of the laser intensity, the pulses with a FWHM beam diameter of approximately 50 mm are guided into the target chamber and then eventually focussed onto the target by an off-axis parabolic mirror.

## 3.2 Electron Acceleration Setup and Diagnostics

The setup for the electron acceleration experiment as carried out in September 2010 as well as the convention for the coordinate system of the target chamber is depicted in Figure 3.3.

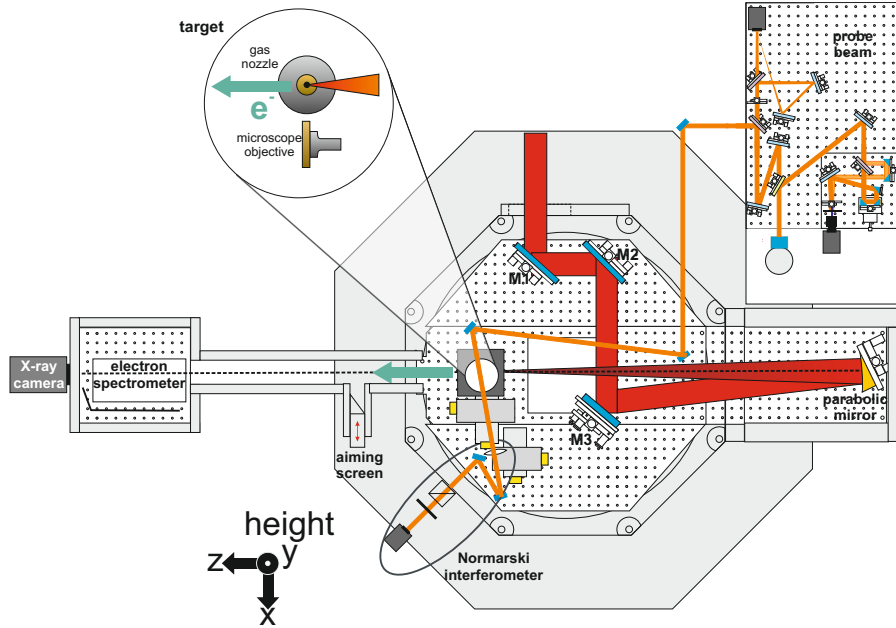


Figure 3.3: The main beam (red) is focused with a parabolic mirror ( $f=1020.8$  mm) into a gas jet. The energy distribution of the accelerated electrons is measured in the electron spectrometer. For each shot, the probe beam (orange) propagating nearly perpendicular with respect to the main beam records the electron density distribution along its way through the plasma. Using a Normarski interferometer, the phase of the probe beam and thus, the integrated refractive index of the plasma (see also Chapter 4), is imaged with a CCD camera. The pointing of the electron pulse can be determined with a movable aiming screen. An X-ray CCD was used to image betatron radiation emitted by the electrons oscillating perpendicularly to the laser axis.

Employing an off-axis parabolic mirror with a focal length of 1020.8 mm, the main beam is focused into a gas jet. Combined with a FWHM beam diameter of 50 mm, an f-number of 20 is obtained. The laser axis is defined in z-direction. A probe pulse propagates through the ionized gas nearly perpendicular with respect to the laser axis. Hence, the plasma density can be investigated as explained in chapter 4. Simultaneously, the energy distribution of the accelerated electrons is determined in the electron spectrometer. For data acquiring and step

motor control Labview<sup>1</sup> routines were used.

### 3.2.1 Setup and Characterization of the Probe Beam

The interaction of the main beam with a medium, such as gases metals or glass, can be investigated with a probe beam. Applying a delay stage, the plasma generated by the laser pulse can be investigated at different times with respect to the main pulse arrival. Thus, the temporal evolution of this perturbation is measurable. To provide temporal synchronization of the pulses, the probe pulse is split from the main pulse at a dielectric mirror. In addition to the mandatory components, new features, a single shot autocorrelator as well as near and far field diagnostics, are integrated (section 3.2.1). A photograph of the probe beam setup is shown in Figure 3.4.

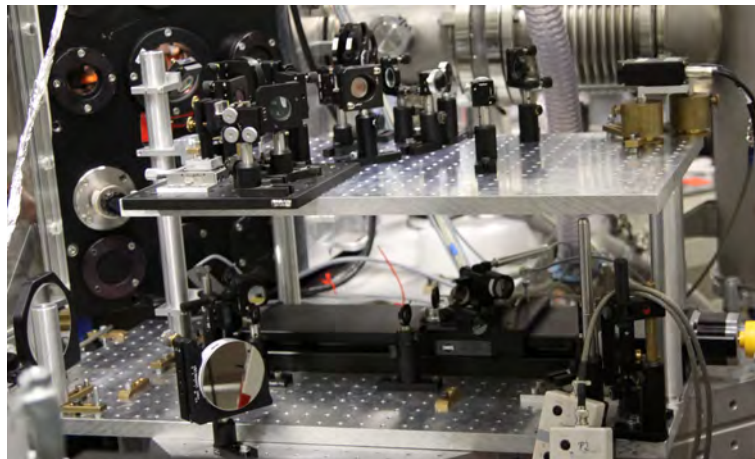


Figure 3.4: The probe beam is set up on two platforms. A mirror telescope and a linear translation stage representing the main components are situated on the lower platform. Near and far field diagnostics as well as a single shot autocorrelator are integrated on the upper platform.

In dependence on the pulse duration and the diameter of the plasma, the temporal resolution of the measurement can be influenced while the spatial resolution is given by the f-number of the lens and the wavelength of the pulse. As the interferogram is imaged with a CCD camera, the resolution can be limited technically. To avoid this, the pixel size has to be chosen sufficiently small and the magnification of the lens sufficiently high.

---

<sup>1</sup>LABORATORY VIRTUAL INSTRUMENTATION ENGINEERING WORKBENCH

## CHAPTER 3. EXPERIMENTAL SETUP AND METHODS

Due to the upgrade of the JETI-laser system in autumn 2009, the pulses have a broader spectrum and hence, the transform limited pulse duration is shorter (see table 3.1).

|                | previous | after upgrade |
|----------------|----------|---------------|
| bandwidth      | 12 nm    | 35 nm         |
| pulse duration | 80 fs    | 27 fs         |

Table 3.1: Overview on FWHM bandwidth and FWHM pulse duration before and after the upgrade of the laser system.

For this reason, dispersion is more significant and has been taken into account for the setup of the new probe beam. Furthermore, it has to be possible to probe the interaction area before and after the main pulse has passed. Usually, in experiments, the main pulse is focused with a parabolic mirror. To fulfill this requirement for parabolic mirrors with small focal distances (120mm), the optical path of the probe beam has to be minimized. For experiments employing parabolic mirrors with large focal distances (1020.8mm) an additional constant delay line must be installable.

### Setup

The probe beam is set up on two platforms. After the probe pulse is split from the main pulse, it is coupled in on the lower platform (Figure 3.5).

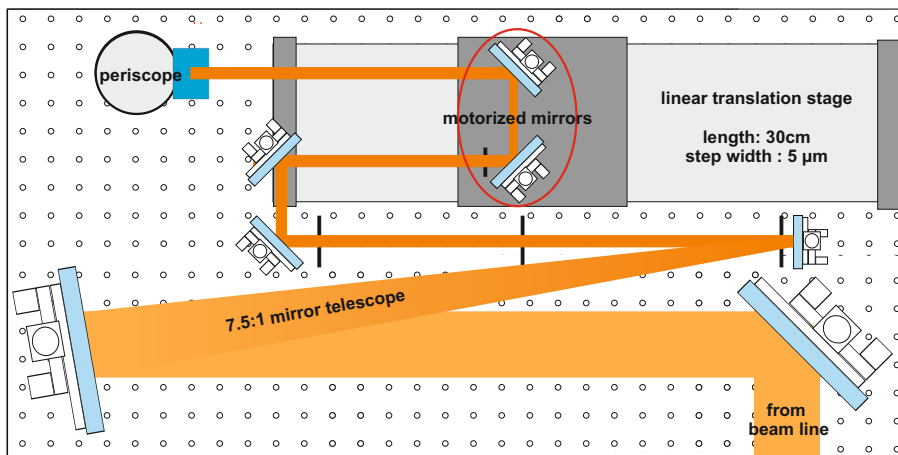


Figure 3.5: Probe beam setup: lower platform. The probe beam is coupled in, telescoped down and delayed with regard to the main beam.

To avoid dispersion, the lens telescopes of the former probe beam have been replaced by a 7.5 : 1 mirror telescope reducing the beam diameter to about 6.7 mm. The beam path of the probe pulse is determined by the path of the main beam. Therefore, the focal lengths of the telescope mirrors are restricted. The 4'' mirror has a focal length of 750 mm and the 1'' mirror one of  $-100$  mm. Combined with a laser beam diameter of 50 mm at the entrance and 6.7 mm at the exit of the telescope, the aperture ratio of the telescope mirrors amounts to 15. Nevertheless, aberrations are magnified since the curvature of the wave fronts is increased when the beam diameter is reduced. As the large telescope mirror is not an off axis one, the telescope has to be set up at an angle the size of which is a compromise between keeping the resulting astigmatism as small as possible and avoiding to block the beam with the coupling-in mirror.

By means of a 300 mm linear translation stage, the temporal delay between main and probe pulse can be varied. Its minimal step width of  $5 \mu\text{m}$  corresponds to a minimal temporal delay of 33 fs since the probe beam has to pass the delay line twice, i.e., the 300 mm translation stage covers a time window of 2 ns. It has been observed that the linear translation stage shows inaccuracies when it is moved<sup>37</sup>. For this reason, the probe beam experiences a displacement in dependence on the position of the translation stage (section 3.2.1). To compensate for the direction of the probe pulse, one of the mirrors of the translation stage of the former probe beam was motorized. This concept has been adapted and extended by additionally motorizing the second mirror of the translation stage. Hence, in addition to the beam direction the beam position can be readjusted remotely.

The two platforms are connected via periscope. On the upper platform (Figure 3.6), the pulses can be coupled out for pump-probe experiments. Moreover near and far field diagnostics as well as a single shot autocorrelator are installed for beam characterization.



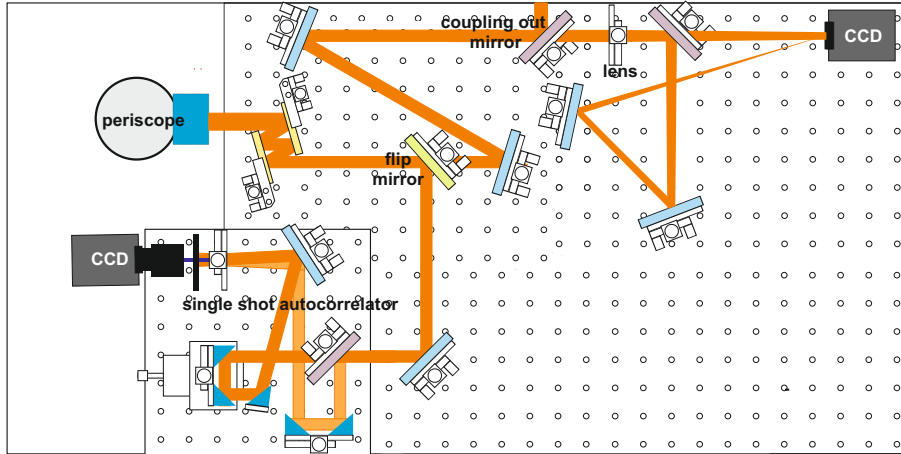


Figure 3.6: Probe beam setup: upper platform. The probe pulses are coupled out for experiments and can be characterized using near and far field diagnostics and a single shot autocorrelator.

### Features

**Near and Far Field Diagnostics.** The lateral beam displacement caused by the translation stage can be quantified imaging near and far field of a beam. The near field is a parallel beam representing the beam position while the far field is situated in the focus of the beam and corresponds to the beam direction.

For these measurements, laser light leaking through the coupling out mirror on the upper platform of the probe beam is utilized. To detect near and far field of a pulse with a small CCD chip, it is focused with a lens. Afterwards, the beam is split at a 1 mm thick glass plate. If

$$\frac{\eta D^4}{16\lambda z_0^3} > 1 \quad (3.1)$$

holds a beam is in the near field<sup>11</sup>. Considering a refractive index of  $\eta=1$ , an aperture of the focusing lens of  $D=2.54$  cm, a wavelength of 800 nm and a distance of the camera from the lens of  $z_0=20$  cm for the transmitted part (N), the ratio amounts to 4.1 and therefore, N represents the near field. The reflected part (F) covers a larger distance and is focused onto the camera (Figure 3.7(a)) representing the far field. An image of near and far field of a beam is shown in Figure 3.7(b).

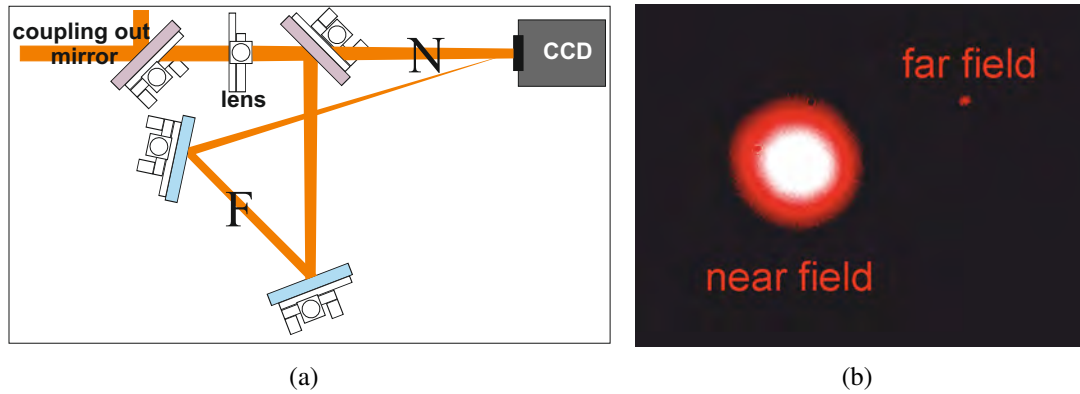


Figure 3.7: The setup of near and far field diagnostics is depicted in (a). A pulse propagates through an imaging lens and subsequently, is split at a glass plate. Near (large spot) and far field (small spot) are depicted in (b).

The displacement of the far field has been measured with a helium-neon laser. The vertical displacement (Figure 3.8(a), black line) exhibits a linear slope, i.e. it depends on adjustment. In contrast, the horizontal beam displacement (Figure 3.8(b), black line) is not connected linearly to the position of the translation stage. It was found that the translation stage is tilted horizontally when it moves. The beam displacement can be compensated readjusting near and far field to their original position (Figure 3.8 violet lines).

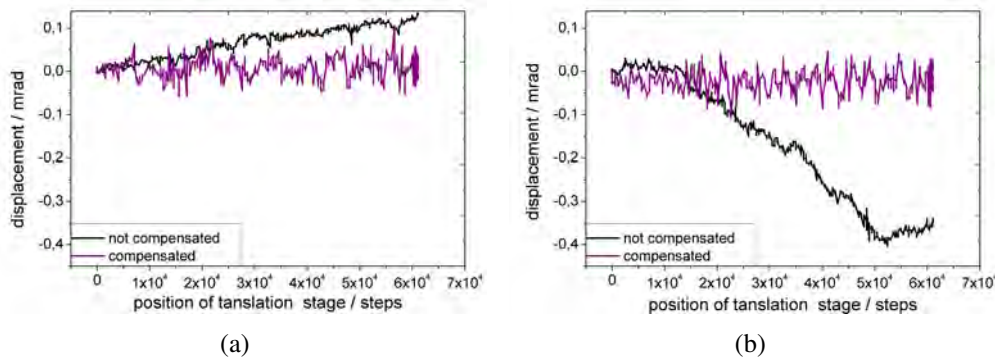


Figure 3.8: The vertical beam displacement (a) depends on adjustment while the horizontal beam displacement (b) additionally depends on the position of the translation stage (black lines). Employing the motorized mirrors of the translation stage, the beam displacement can be compensated (violet lines). The accuracy of the readjustment amounts to about  $\pm 0.1$  mrad for this measurement.

By means of a self developed Labview routine, the motorized mirrors of the translation

stage can be controlled remotely. As the mirror movement is not reproducible exactly, the routine adjusts the mirrors iteratively. The software has access to the original and the current position of near and far field so that automatic readjustment is possible. The accuracy of the adjustment depends on the stability of the pointing of the incident beam and the pixel size of the imaging camera. For the measurement in Figure 3.8 an accuracy of  $\pm 3$  px corresponding to approximately  $\pm 0.1$  mrad was chosen. Due to the stable pointing of the helium-neon laser used for this measurement it would have been possible to further increase the accuracy to about  $\pm 0.03$  mrad. However, the pointing of the probe beam inside the target chamber is less stable as it is subject to vibrations generated by the vacuum pumps. An accuracy of approximately  $\pm 150$  mrad and  $\pm 50$  mrad for the near and the far field, respectively is feasible.

**The Single Shot Autocorrelator.**

The pulse duration of the probe beam has not been measured for the previous setup. Measuring the duration of the probe pulse introduces the possibility to compress the pulse to its transform limit using dispersive mirrors as long as the pulse did not experience higher order dispersion.

The pulse coupled into the single shot autocorrelator (Figure 3.9) is split into two replica at a beam splitter.

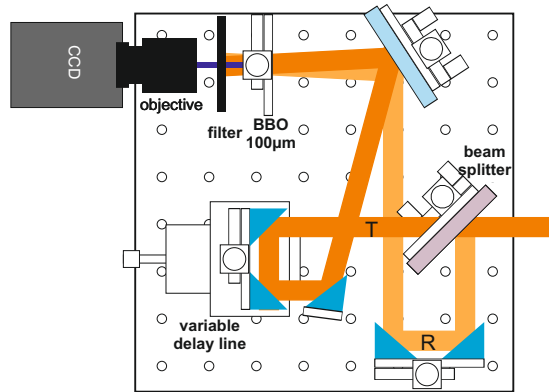


Figure 3.9: Setup of the single shot autocorrelator. Measuring the width of the second harmonic generated in the BBO crystal, the pulse duration of the incoming pulse can be calculated.

The transmitted pulse (T) passes a variable delay line so that it can be shifted temporally with respect to the reflected one (R). As the delay line s has to be covered twice by the trans-

mitted pulse, the corresponding shift in time  $\Delta t$  can be calculated as

$$\Delta t = \frac{2s}{c} \quad (3.2)$$

where  $c$  is the velocity of light. The second harmonic of the two pulses generated in a  $100 \mu\text{m}$  thick BBO crystal passes a filter blocking the remainders of the fundamental frequency and is imaged at a CCD camera. The nonlinear crystal has been tested with pulses as short as 27 fs comparing the pulse duration measured with the crystal with the one measured employing a commercially acquirable device<sup>1</sup>.

The pulse duration of the probe beam measured using the single shot autocorrelator was compared to theory. To process the theoretical calculations Lab2<sup>38</sup> was used. Lab2 is an add-on to Labview developed to simulate experiments in ultra fast optics. To accurately calculate the theoretical pulse duration, the spectrum of the probe beam (Figure 3.10, black line) has been measured. Comparing the spectra of the probe and the main beam (Figure 3.10, violet line), it can be recognized that these are not identical. Presumably, the spectrum of the probe pulse is modified when the pulse is transmitted through the beam splitter.

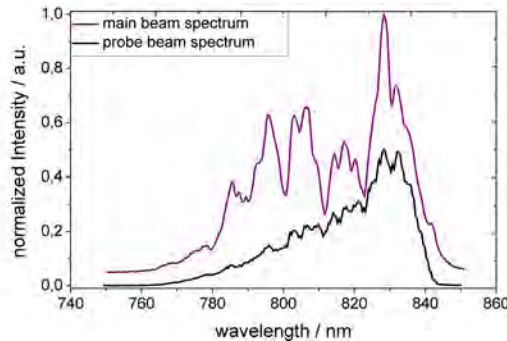


Figure 3.10: Spectra of the main (violet) and the probe beam (black). Each spectrum is normalized to an arbitrary value. As the probe beam is split from the main beam as 1 : 99, its maximal intensity is not more than 1/99 of the maximal intensity of the main beam.

For interferometric measurements, temporal as well as spatial coherence have to be provided. Temporal coherence is connected to the width of the spectrum of the radiation. The broader the spectrum the less interference stripes are visible. Figure 3.11(a) depicts an interferogram recorded with the broad probe beam spectrum. In this case, few interference

---

<sup>1</sup>FEMTOMETER from FEMTOLASERS

stripes appear whereas interferometry with the probe beam spectrum filtered with an adequate interference filter increases the number of stripes (Figure 3.11(b)). Disadvantageously, the temporal resolution is lower for a cut spectrum.

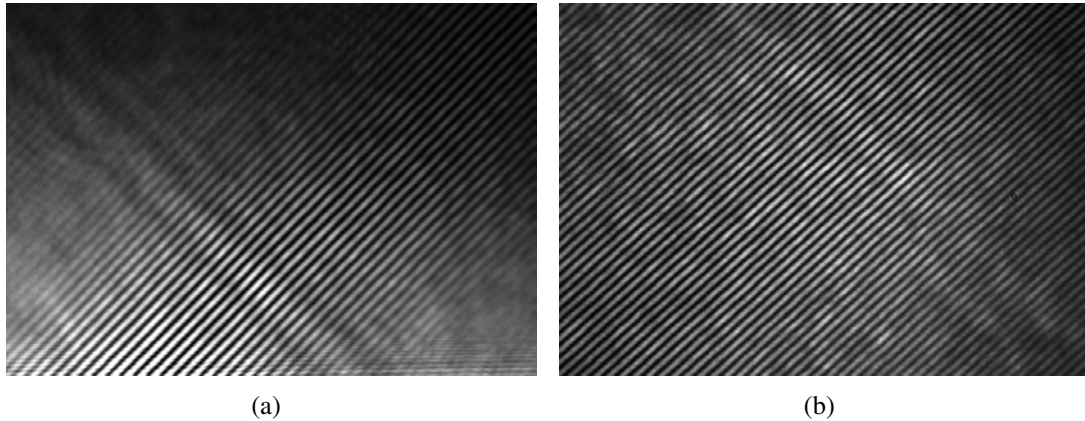


Figure 3.11: Interferograms of the (a) broad and (b) cut probe beam spectrum. To cut the spectrum a 10 nm bandpass filter was used. The broader the spectrum the lower the number of interference stripes.

The filtered spectrum (violet line) is depicted in comparison to the probe beam spectrum (black line) in Figure 3.12(a). Employing these spectra, the filter function can be calculated. Fitting a Gaussian function to the filter data (Figure 3.12(b)) yields a FWHM of 10,5 nm centered at 800 nm.

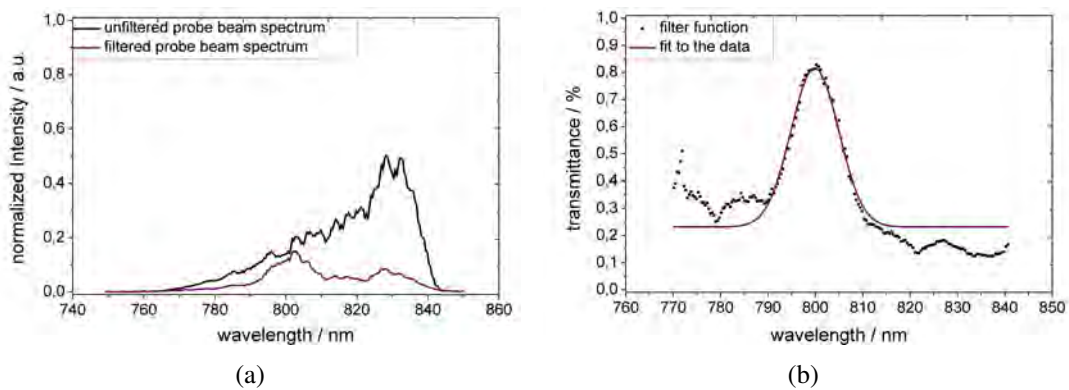


Figure 3.12: The filtered (violet) and unfiltered spectrum (black) at the tapping for the probe beam is depicted in (a). Again, each spectrum is normalized to an arbitrary value. The calculated filter function (black dots) and Gaussian fit to the data (violet line) (b) can be determined up to a factor of proportionality.

The transform limited as well as the pulse duration due to dispersion have been calculated and measured for the filtered and the unfiltered spectrum of the probe beam.

**Theory.**<sup>1</sup> As the spectra do not have a Gaussian shape (Figure 3.10, Figure 3.12(a)), the transform limited pulse duration is not that of a Gaussian pulse. In the following, the bandwidth is given as the full width at 10% of the maximal intensity. The transform limited pulse duration of the main beam is 27.1 fs at a spectral width of 66.5 nm. For a bandwidth of about 59.9 nm of the uncut spectrum of the probe beam together with the intensity in dependence on the wavelength, the transform limited pulse duration expected amounts to 28.6 fs. To account for the interference filter used in the experiment, the filtered spectrum is used for calculations. The bandwidth of the filtered spectrum amounts to 59.1 nm. Before the probe beam traverses the plasma it passes several dispersive media. The unfiltered pulse is stretched to 98.3 fs and the filtered one to 217.6 fs.

A vacuum window has to be passed by the probe beam to enter the target chamber. In the experiment it was a Quartz window of a thickness of 10 mm. Considering this to calculate the pulse duration inside the chamber, the initially short pulse of 27.4 fs has a duration of 113.5 fs at the target.

The inaccuracy of the spectrometer used to measure the spectra of the probe beam is about 1 nm and therefore, it does not significantly affect the calculation of the respective pulse durations.

**Measurement.** To calibrate the measurement, the images of the second harmonic were taken for four relative delays between the reflected and the transmitted pulse. The linear translation stage of the autocorrelator was displaced by 80  $\mu\text{m}$  corresponding to a total temporal displacement of 533 fs. As explained in section 2.1.4 the position of the signal of the second harmonic shifts on the image in dependence on the delay between the two pulses. The total temporal delay between the two pulses exceeds the maximum pulse duration by more than 100% justifying the usage of the calculated calibration factor. Figure 3.13 depicts the images used for calibration.

---

<sup>1</sup>Calculated using Lab2<sup>38</sup>

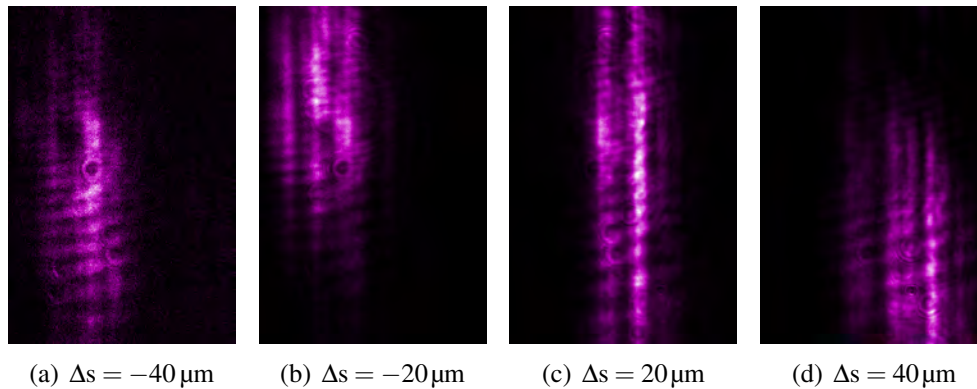


Figure 3.13: Calibration images. As the fundamental beams are coherent interference stripes are visible in the second harmonic.

Fitting the relative delay to the position of the maximal intensity gives the calibration factor (Figure 3.14). It is determined for this setup as  $4.6 \pm 0.08$  fs/px.

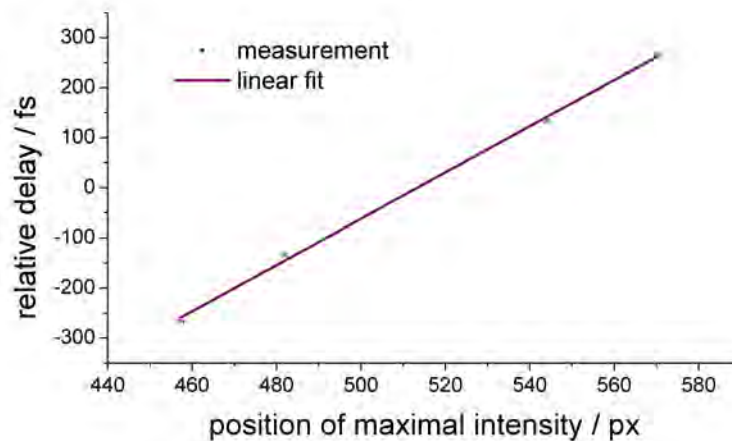


Figure 3.14: Linear fit of the temporal delay between the two pulses over the pixel number of the position of the maximum intensity. The slope yields a calibration factor of  $4.6 \pm 0.08$  fs/px.

To obtain the pulse duration from the width of the second harmonic, equation 2.20 is used. Due to the propagation of the probe beam through dispersive media, the pulse duration was measured to be  $87 \pm 6$  fs. An interference filter with a transmittance bandwidth of 10 nm centered at 800 nm further stretches the pulse duration to  $183 \pm 11$  fs (Figure 3.15).



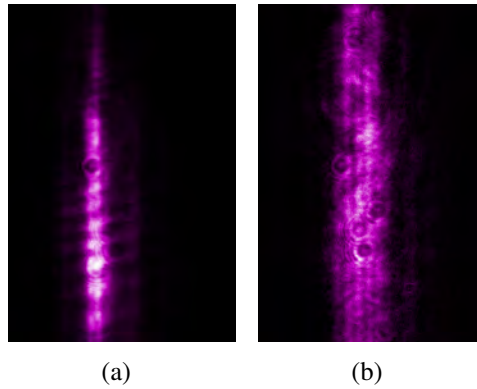


Figure 3.15: Second harmonic signal to determine the pulse duration for (a) the unfiltered and (b) the filtered spectrum.

**Comparison** Measurement and calculation are compared graphically in Figure 3.16. Especially for the unfiltered spectrum theoretical and experimental results are in good agreement.

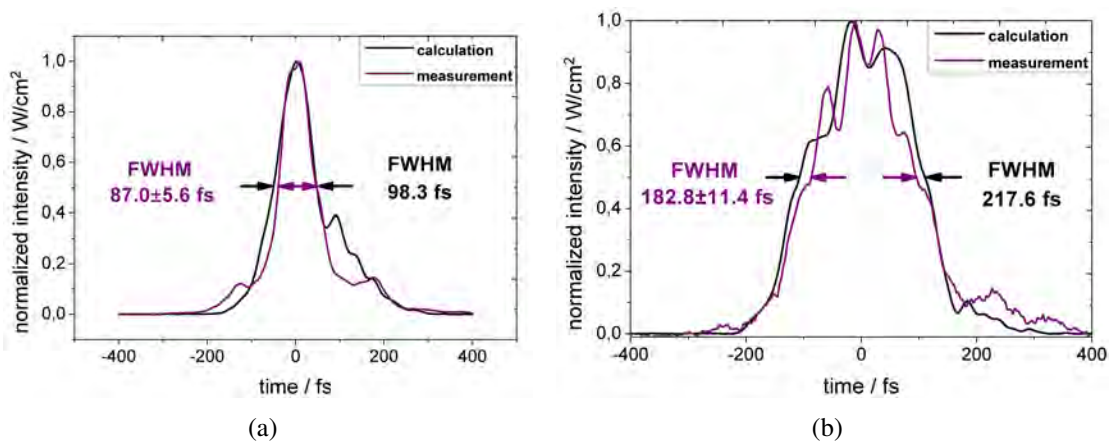


Figure 3.16: Comparison of theory and measurement for (a) the broad and (b) the cut spectrum.

As the inaccuracy for the theoretical values is negligible, only the inaccuracies of the measured ones are considered. The pulse with the uncut spectrum has a measured pulse duration of  $87 \pm 6$  fs while it was calculated to 98 fs. The difference between measurement and theory is less than 10% and in the range of the inaccuracy due to the measurement. Calculating the duration with the filtered spectrum gives a pulse duration of 218 fs. However, the measured pulse duration amounts to  $183 \pm 11$  fs. The material of the interference filter is not known. For this reason, the discrepancy between theory and measurement is larger than the calculated



inaccuracy. Furthermore, the relative inaccuracy is higher for the pulse with the filtered spectrum than for the one with the unfiltered spectrum.

### 3.2.2 The Normarski Interferometer

To generate a probe and a reference from an incident beam, in a Normarski interferometer a Wollaston prism (Figure 3.17) is used. It consists of two birefringent quartz prisms whose optical axes are oriented perpendicularly to each other. As a result, a pulse incident with its plane of polarization oriented under  $45^\circ$  with respect to these axes is separated by the prism into two beams with polarization perpendicular to each other but with the same intensities. Both of the beams cover the same optical path providing temporal coherence intrinsically. Therefore, it is very well suited for short pulse interferometry.

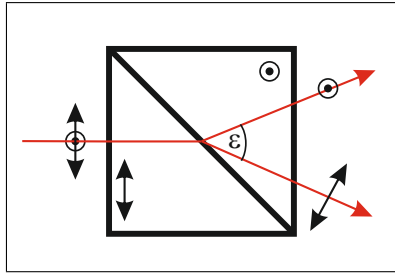


Figure 3.17: The optical axes of the two birefringent prisms of the Wollaston prism are oriented perpendicularly to each other. A beam with its plane of polarization oriented under  $45^\circ$  with respect to these axes is split into two beams with a polarization perpendicular to each other.

Next to temporal coherence, for interferometry also spatial coherence is required. The distance along which the two beams have to be spatially coherent<sup>7</sup>

$$d_c = \frac{\Delta x_{wi} \epsilon}{V} \quad (3.3)$$

depends on the magnification of the lens  $V$ , the distance of the image plane from the Wollaston prism  $\Delta x_{wi}$  and the angle  $\epsilon$  between the two beams.  $\epsilon$  is determined by the angle between the plane of incidence and the mating surface as well as the difference in the two refractive indices. To allow interference between the two beam parts, a polarizer is included after the prism.

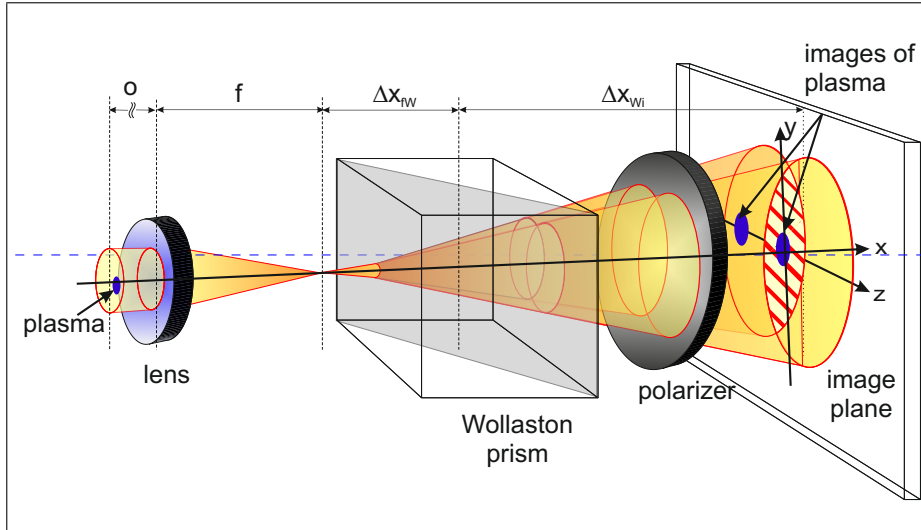


Figure 3.18: Normarski interferometer. A lens is situated in a distance  $o$ , from the plasma. Inside the Wollaston prism the beam is split symmetrically. A polarizer allows for interference of the beams whose polarization is oriented perpendicular to each other.  $\Delta x_{fW}$  denotes the distance between the focus of the lens and the Wollaston prism while  $\Delta x_{Wi}$  is the distance from the prism to the image plane.

The width of the interference stripes is given by<sup>7</sup>

$$d_s = \frac{\lambda}{\varepsilon} \cdot \frac{\Delta x_{Wi}}{\Delta x_{fW}} \quad (3.4)$$

with the wavelength of the incident radiation  $\lambda$  and the distance between the focus of the lens and the Wollaston prism  $\Delta x_{fW}$ , i.e. the distance of the stripes can be varied through the position of the prism.

Phase changes induced by the electron density distribution are contained in both beams. To obtain an interferogram from which the phase shift can be retrieved, a part of the beam containing the plasma signal (probe), i.e. a disturbance, is superimposed with an undisturbed area of the other beam (reference)<sup>39</sup>.

### 3.2.3 The Electron Spectrometer

The electron spectrometer (Figure 3.19) used in the experiment was built in 2006<sup>40</sup>. Due to recent changes in the scope of a Diploma thesis<sup>28</sup>, the energy scale of the spectrometer has been

recalculated. In a magnetic field, charged particles are forced into a circular trajectory around the magnetic field lines if they have a velocity component perpendicular to the magnetic field. The higher the energy of an electron with the mass  $m_e$  the larger is the radius of curvature. To measure the electron energy, a phosphorescent material is installed (Figure 3.19(b)). The number of electrons incident at such a screen is proportional to the intensity of the emitted radiation<sup>41</sup>.

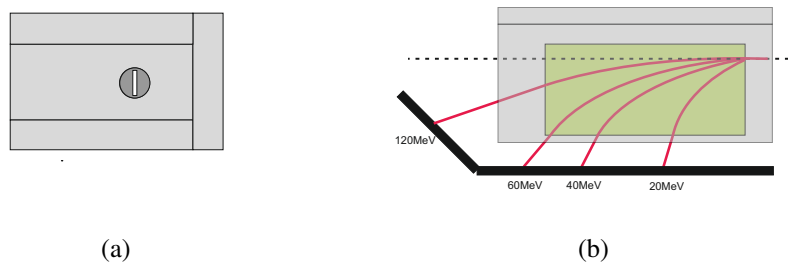


Figure 3.19: The electron spectrometer is depicted (a) from the front with a 2 mm slit oriented perpendicularly to the plane of dispersion and (b) from the top with the phosphorescing screens (black) and electron trajectories for different electron energies (red). The dashed line is the trajectory of an electron in the absence of a magnetic field..

The electron bunch accelerated inside a bubble exhibits divergence (section 2.2.5). Depending on the angle of divergence, the energy resolution is affected. A vertical slit with a width of 2 mm at a distance of one meter from the target reduces the angle of divergence to<sup>1</sup> 1 mrad. Moreover, the energy resolution is affected by the nonlinear relation of electron energy and the curvature of the electron trajectory. The higher the electron energy the lower the energy resolution. To measure in a sufficient energy range, *low* (10 – 55 MeV) and *high energy* (60 – 240 MeV) electrons are detected at separate screens.

<sup>1</sup>Half opening angle.

## 4 Interferometric Plasma Probing

In this chapter, the relation between the interferograms, the probe beam phase and the electron density distribution is explained. To yield the electron density distribution from the interferograms, Fourier transformation and Abel inversion are well-established methods.

### 4.1 Electron Density and Phase of the Probe Beam

Assuming the plasma to be investigated is sufficiently thin and the density gradient sufficiently low, the probe beam is not refracted but only accumulates additional optical phase compared to a propagation in vacuum. The phase shift difference  $\Delta\Phi$  the beam experiences in the plasma is an indicator for the refractive index distribution  $\eta(x, y, z)$  of the plasma which in turn is connected to the electron density distribution  $n_e(x, y, z)$  (equations 4.1 - 4.5). Figure 4.1 illustrates a possible electron density distribution and the corresponding phase shift of the probe pulse.

Considering a plane  $z = \text{const}$ , i.e. perpendicular to the direction of main-pulse propagation, and the probe beam to propagate in  $x$ -direction, the refractive index of a plasma is a two dimensional distribution  $\eta(x, y)$ . For each height  $y_i$ , the probe beam accumulates the phase shift caused by the plasma along its path in  $x$ -direction. The phase of the probe beam can be expressed in terms of the integrated refractive index<sup>42</sup>

$$\Phi(y_i) = \frac{\omega}{c_0} \int (\eta(x, y_i)) dx. \quad (4.1)$$

This equation represents the sum of the undisturbed phase an electromagnetic wave accumulates in vacuum, which is linear, and the phase shift caused by the plasma. Subtracting the

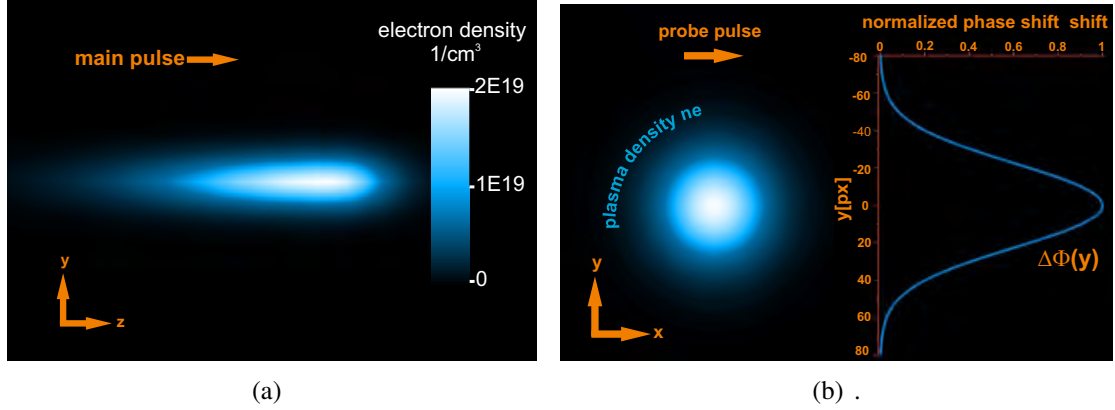


Figure 4.1: The propagation of the probe beam through the electron density distribution of the plasma causes a shift in its phase compared to a vacuum propagation. (a) Radial profile of the electron density along the laser axis. (b) Cross section of the Gaussian shaped electron density perpendicular to the laser axis and the corresponding phase shift  $\Delta\Phi$ . The legend in (a) is also valid for (b)

linear phase of equation 4.1 and plugging in

$$\eta(x, y) = \sqrt{1 - \frac{n_e(x, y)}{n_{cr}}} \quad (4.2)$$

yields

$$\Delta\Phi(y_i) = \frac{\omega}{c_0} \int \left( \sqrt{1 - \frac{n_e(x, y_i)}{n_{cr}}} - 1 \right) dx \quad (4.3)$$

describing the phase shift of the probe beam in dependence on the integrated electron density. Assuming  $n_e \ll n_{cr}$ , the square root in equation 4.3 can be approximated Taylor expanding until the linear term

$$1 - \frac{1}{2} \cdot \frac{n_e(x, y_i)}{n_{cr}} \quad (4.4)$$

and equation 4.3 can be transformed to

$$\Delta\Phi(y_i) \approx \frac{\omega}{2c_0 n_{cr}} \int n_e(x, y_i) dx. \quad (4.5)$$

Thus, the integrated plasma density is related to the phase shift difference measurable interferometrically.

## 4.2 Phase Measurement

In a Normarski interferometer (section 3.2.2) an incident pulse is split into two replica which can be described by  $\mathcal{E}_I \cdot \exp(i\omega t)$  and  $\mathcal{E}_{II} \cdot \exp(i\omega t + i\Delta\Phi)$ , respectively. Coherently superimposing the two waves leads to a resulting field of

$$\mathcal{E}_{\text{res}} = (\mathcal{E}_I + \mathcal{E}_{II} \cdot \exp(i\Phi)) \cdot \exp(i\omega t) \quad (4.6)$$

and a corresponding intensity of

$$I_{\text{res}} \propto \mathcal{E}_{\text{res}}^2 = \mathcal{E}_I^2 + \mathcal{E}_{II}^2 + 2\mathcal{E}_I \mathcal{E}_{II} \cos \Phi \quad (4.7)$$

which can be imaged using a CCD camera. The intensity distribution due to interference of the two pulses is depicted in Figure 4.2. While superimposing two undisturbed parts gives straight stripes (Figure 4.2(b)), the interference pattern exhibiting the plasma information shows bent stripes 4.2(a).

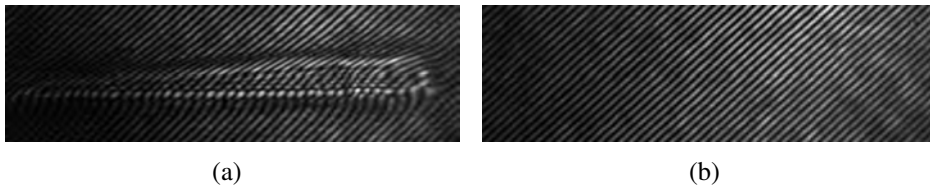


Figure 4.2: Interference patterns for (a) an interferogram containing plasma information and (b) the corresponding reference interferogram in vacuum. Whereas the perturbation due to the plasma leads to bend interference fringes, the reference interferogram shows straight stripes.

As the cosine is  $2\pi$ -periodic, it is not possible to retrieve the absolute phase  $\Phi$ . To work around this, a reference interferogram containing exclusively vacuum phase information is recorded. Instead of calculating the absolute phase shift, the phase of the reference is sub-

tracted from the phase containing the plasma information

$$\Delta\Phi = \Phi_{\text{plasma}} - \Phi_{\text{vacuum}} = \frac{\omega}{c} \int (\eta - 1) dx. \quad (4.8)$$

This equals equation 4.1 and can be transformed into a dependency of the phase shift on the integrated electron density (equation 4.5). If no reference interferogram is available, alternatively, one can calculate the plane phase originating from vacuum by fitting a plane on the phase information of the measurement interferogram and subtracting this from the measured phase.

## 4.3 Phase Retrieval

### 4.3.1 Removal of Disturbing Frequencies from the Interferogram via Fourier Filtering

The two dimensional intensity distribution<sup>43</sup>  $I(x, y)$  of an interferogram can be described by

$$I(x, y) = \tilde{I}(\vec{r}) = \tilde{I}_0(\vec{r}) + \tilde{C}(\vec{r}) \cos(2\pi\vec{v}_0(\vec{r})\vec{r} + \Phi(\vec{r})). \quad (4.9)$$

$I_0$  is the background intensity and  $\vec{v}_0$  the carrier frequency vector. The contrast function  $C(\vec{r})$  indicates the visibility of the interference stripes. Substituting

$$\tilde{A}(\vec{r}) = \frac{1}{2} \tilde{C}(\vec{r}) e^{i\Phi} \quad (4.10)$$

in equation 4.9 yields

$$\tilde{I}(\vec{r}) = \tilde{I}_0(\vec{r}) + \tilde{A}(\vec{r}) e^{2\pi i \vec{v}_0 \vec{r}} + \tilde{A}^*(\vec{r}) e^{-2\pi i \vec{v}_0 \vec{r}} \quad (4.11)$$

where  $\tilde{A}^*$  denotes the complex conjugate of  $\tilde{A}$ . Fourier transforming this equation results in

$$\tilde{i}(\vec{r}) = \tilde{i}_0(\vec{v}) + \tilde{a}(\vec{v} - \vec{v}_0) + \tilde{a}^*(-\vec{v} - \vec{v}_0) \quad (4.12)$$

with a small letter representing the Fourier transformed of the quantities labeled with the corresponding capital letter. Transformed into the frequency domain, the phase function  $\Phi$  is separated from the intensity background  $\tilde{i}_0$  by the carrier frequency  $\vec{v}_0$ . Shifting the lower frequency components to the center of the spectrum, the required phase information is arranged symmetrically around the low frequencies of the background intensity as depicted in Figure 4.3(a). To filter the phase information contained in  $\tilde{a}$  or  $\tilde{a}^*$ , respectively, the Fourier spectrum is masked.

Backtransforming the masked data to the spatial domain, returns the function  $A(\vec{r})$  exhibiting the data of the cleaned interferogram shown in Figure 4.3(b).

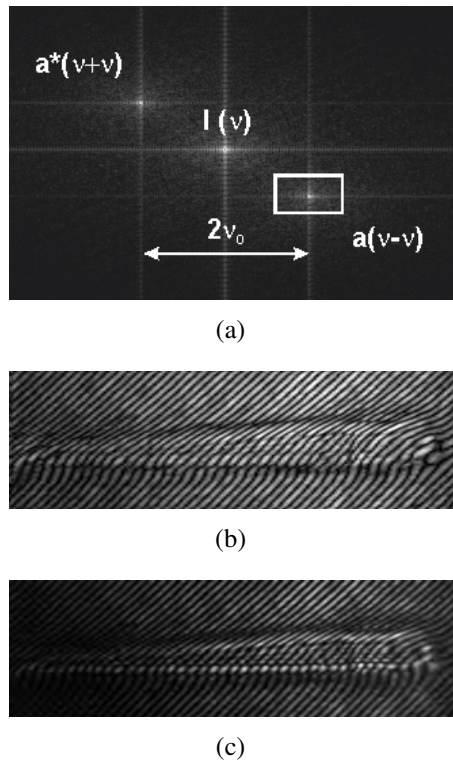


Figure 4.3: Data in the Fourier and spatial domain. In the cut-out of the FFT data (a) the area outside the white contoured rectangle is masked. All the data outside the rectangle are set to zero. The data of the interferogram edited in the Fourier domain (b) is suited for phase retrieval. For comparison, the original interferogram is shown in (c).



### 4.3.2 Phase Calculation

The phase of the probe beam can be calculated by means of

$$\Phi(\vec{r}) = \arctan \frac{\text{Im}(A(\vec{r}))}{\text{Re}(A(\vec{r}))}. \quad (4.13)$$

If the phase information  $a(\vec{v} - \vec{v}_0)$  is filtered when the lower frequency components are not shifted to the center of the spectrum, equation 4.13 contains a linear phase that has to be removed to yield the desired information. Due to the  $2\pi$ -periodic discontinuities of the arctan-function, the phase cannot be retrieved uniquely in the first place but has to be unwrapped to obtain a continuous phase function. The phase jumps amounting to an integer multiple of  $2\pi$  can be removed by adding several step functions to the phase function (Figure 4.4).

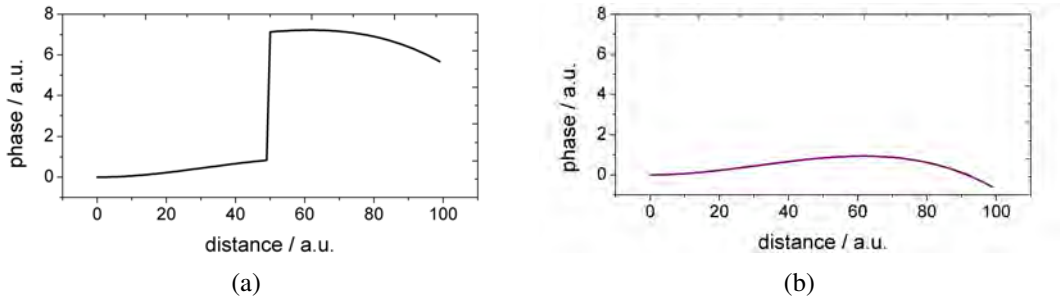


Figure 4.4: The  $2\pi$ -periodic discontinuities of the arctan-function cause phase jumps (a). The unwrapped phase is a continuous function.

If the discrepancy between two adjacent values exceeds  $\pi$ , the unwrapped phase  $\Phi_u$  of an  $m \times n$  phase distribution  $\Phi$  is calculated as follows<sup>44</sup>:

$$\Phi_{u_m}(m, n) = \begin{cases} \Phi(m, n) - \left( \frac{\Phi(m, n) - \Phi(m-1, n)}{2\pi} + 0.5 \right) 2\pi & \text{if } i = 1, \dots, m-1 \\ \Phi(m, n) & \text{if } i = 0 \end{cases} \quad (4.14)$$

$$\Phi(m, n)_u = \begin{cases} \Phi_{um}(m, n) - \left( \frac{\Phi_{um}(m, n) - \Phi_{um}(m, n-1)}{2\pi} + 0.5 \right) 2\pi & \text{if } i = 1, \dots, n-1 \\ \Phi_{um}(m, n) & \text{if } i = 0 \end{cases} \quad (4.15)$$

The unwrapped phase calculated from the data depicted in Figure 4.3(b) is shown in Figure 4.5(a). Removing the linear phase yields Figure 4.5(b).

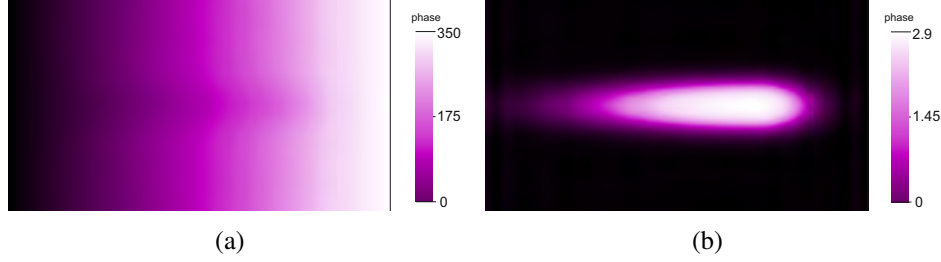


Figure 4.5: Unwrapping the phase obtained with equation 4.13 yields the data depicted in (a). Removing the linear component results in the phase shift of the probe beam (b) caused by the plasma.

## 4.4 Abel inversion

Applying the inverted Abel integral equation to the accumulated phase of the probe beam, the electron density can be calculated.

### 4.4.1 General Idea

Owing to the symmetric distribution of the plasma, the two dimensional projection (equation 4.5) can be traced back to the three-dimensional electron density distribution. For a cylindrically symmetric electron density, Abel inversion can be used to calculate the original distribution. Transforming the differential  $dx$  in

$$\Delta\Phi(y_i) \approx \frac{\omega}{2c_0 n_{cr}} \int n_e(x, y_i) dx \quad (4.16)$$

into cylinder coordinates and inserting it into equation 4.16 gives<sup>42</sup>

$$\Delta\Phi(y) = \frac{\omega}{c_0 n_{cr}} \int_y^R n_e(r) \frac{r dr}{\sqrt{r^2 - y^2}}. \quad (4.17)$$

Abel inverting equation 4.17, the radial electron density distribution<sup>42</sup> (Figure 4.6)

$$n_e(r) = -\frac{\lambda n_{cr}}{\pi} \int_r^R \frac{d\Delta\Phi(y)}{dy} \frac{dy}{\sqrt{y^2 - r^2}}. \quad (4.18)$$

for a plane  $z = \text{constant}$  can be calculated.

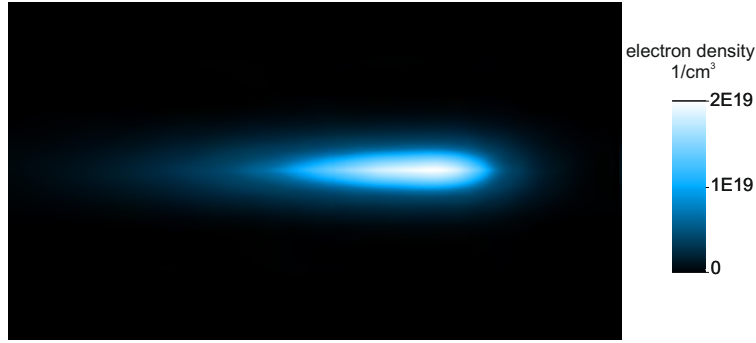


Figure 4.6: Via Abel inversion, the radial electron density distribution can be calculated.

#### 4.4.2 Discrete Abel Inversion

The two dimensional phase shift  $\Delta\Phi$  obtained from the interferograms is not expressed as an analytical function. Rather, the data are available in form of a matrix with discrete elements. For an  $m \times n$  matrix where  $m$  corresponds to  $x$  and  $n$  to  $y$ , the derivative of the discrete values in  $\Delta\Phi(y)$  is calculated as follows<sup>44</sup>

$$\left. \frac{\Delta\Phi(y)}{dy} \right|_{y_i} = \frac{1}{2} (\Delta\Phi(y_{i+1}) - \Delta\Phi(y_{i-1})) \quad (4.19)$$

with  $i = 2, 3, \dots, n - 1$ .

The integral has to be calculated discrete as well<sup>44</sup>:

$$n'_e(r) = -\frac{\lambda n_{cr}}{\pi} \underbrace{\sum_{i=1}^{n-1} \frac{1}{2} \left( \left. \frac{\Delta\Phi(y)}{dy} \right|_{y_i} \frac{1}{\sqrt{y_i^2 - r^2}} + \left. \frac{\Delta\Phi(y)}{dy} \right|_{y_{i+1}} \frac{1}{\sqrt{y_{i+1}^2 - r^2}} \right)}_{\text{Abel inversion}} \quad (4.20)$$

for  $i = 1, 2, \dots, n - 1$ .

In consequence of the discretization of the phase shift due to the pixels of the camera, the electron density  $n'_e(r)$  is given in units of  $1/\text{cm}^3 \cdot \mu\text{m}/\text{px}$  if the wavelength is inserted in  $\mu\text{m}$ .

The electron density  $n_e(r)$  in units of  $1/\text{cm}^3$  is obtained correcting  $n'_e(r)$  with the magnification factor  $M$  of the camera expressed in  $\text{px}/\mu\text{m}$

$$n_e(r) = \frac{n'_e(r)}{M} \quad (4.21)$$

## 5 Results

In this chapter, the electron densities and energies measured in an experiment in the field of laser wakefield acceleration are introduced.

### 5.1 Evolution of the Plasma Density

Electrons can be accelerated close to the speed of light via laser wakefield acceleration. Basically, laser wakefield acceleration takes place in three steps. As soon as the laser intensity is sufficient, the main beam ionizes the gas and thus, generates free electrons. Helium is singly ionized at  $1.4 \times 10^{15} \text{W/cm}^2$  and doubly ionized at  $8.8 \times 10^{15} \text{W/cm}^2$ . Nevertheless, from about  $2 \times 10^{12} \text{W/cm}^3$  free electrons are already generated via tunnel ionization. As the pulses have a peak intensity of about  $10^{19} \text{W/cm}^2$  helium is fully ionized before the peak of the main pulse arrives. The ponderomotive force of the laser pulse causes a plasma wave which generates a longitudinal electric field. If the plasma wave breaks, electrons are injected into a region of low electron density in laser direction and are accelerated in the wakefield of the laser pulse. With a probe pulse, the properties of the plasma at different times during the interaction and hence, during the acceleration process, can be investigated interferometrically. In the experiment, the interferograms were taken with a resolution of  $8 \mu\text{m}$  in propagation direction. Moreover, the probe pulse had a duration of approximately 200 fs causing a blurred image in propagation direction. A plasma wave has a wavelength of few microns. Hence, with this resolution it cannot be resolved. Rather, the measurement gives an average over the electron density which can be calculated from the phase shift of the probe pulse (Figure 5.1(a)). With a probe pulse duration of 8 fs and a spatial resolution of  $2 \mu\text{m}$  A. Buck, M. Nicolai et al. succeeded to resolve the plasma wave (Figure 5.1(b)) via polarimetry.

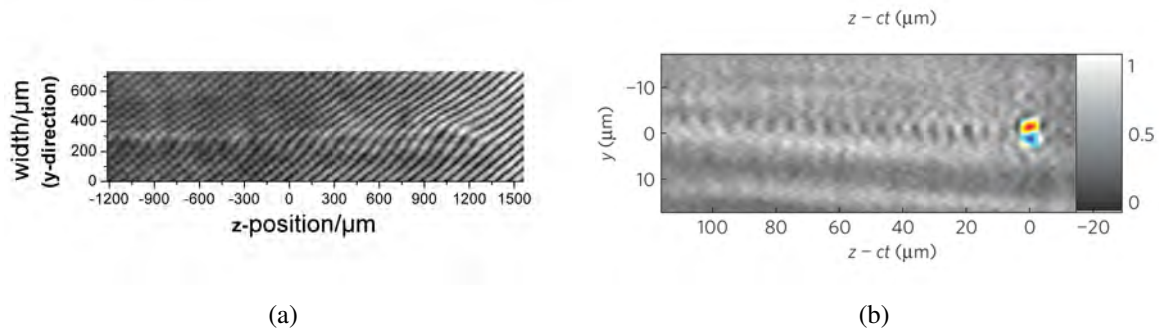


Figure 5.1: Comparison of macroscopic and microscopic measurements. Using a probe pulse with a duration of 200 fs and a spatial resolution of  $8\ \mu\text{m}$ , in the interferogram only the averaged phase of the probe beam can be resolved (a) while with an 8 fs long probe pulse and a spatial resolution of  $2\ \mu\text{m}$  the plasma channel (b) can be resolved by means of polarimetry.

A supersonic gas jet has almost no horizontal velocity component and can be assumed to have a constant gas density along the laser axis<sup>45</sup>, i.e., if the position of one of the edges of the gas jet is known, the position of the middle of the gas nozzle can be estimated: The later the time during the interaction the further the ionization front is shifted in laser direction (Figure 5.2). When the delay of the probe pulse is increased but no further shift of the ionization front is recorded, the rear edge of the gas jet is reached. Subtracting the radius of the gas nozzle from that position the middle of the gas is obtained. The diameter of the gas nozzle was 3 mm in the experiment. In the pictures the middle of the gas jet is situated at position=0. The leading edge was not imaged with the camera.

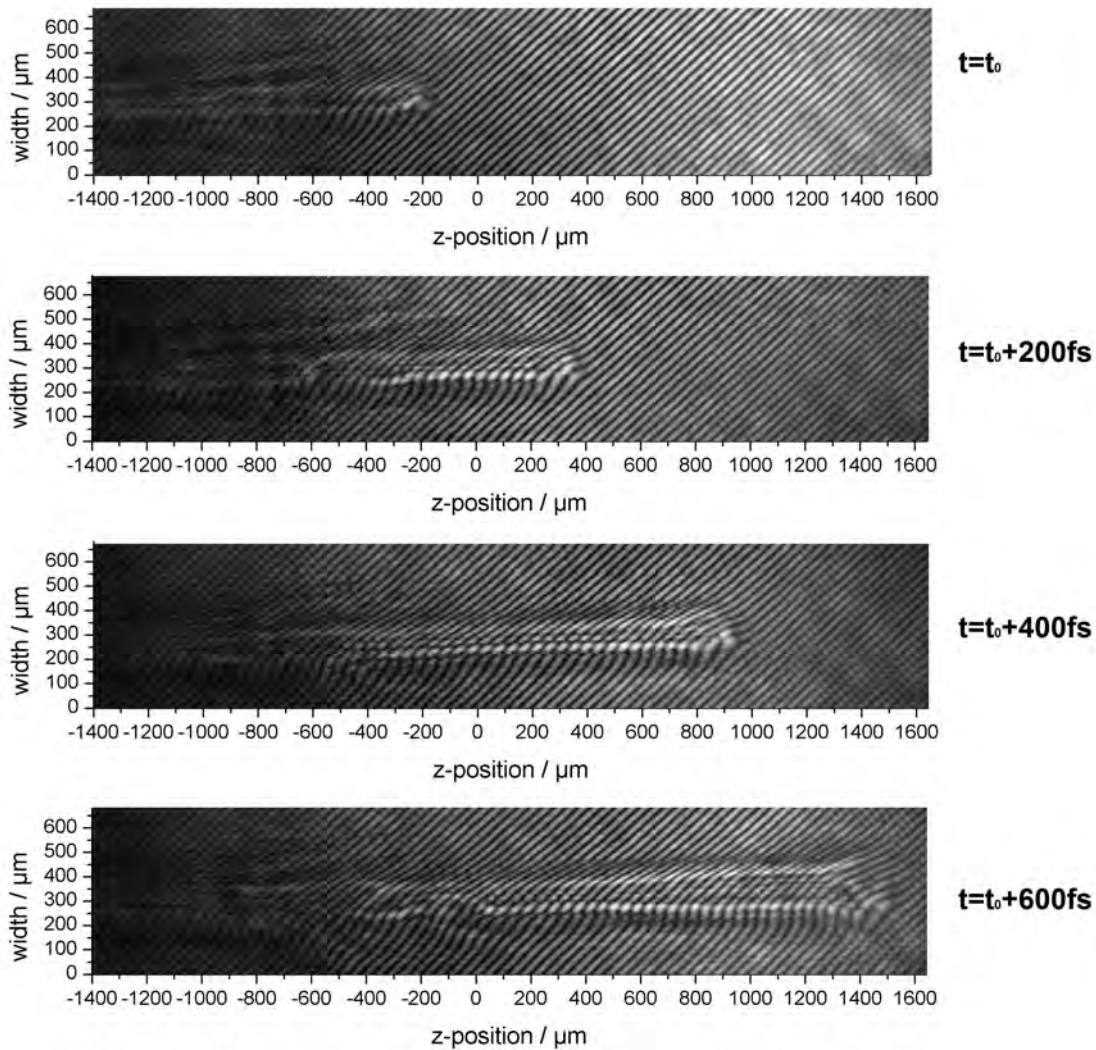


Figure 5.2: The later the probe pulse passes the plasma the further the ionization front has propagated. The interferograms are recorded at different interaction times. From the uppermost to the lowermost picture each interferogram is taken at a later time during the interaction. The middle of the gas nozzle with a 3 mm diameter is situated at position = 0.

Since the phase of the probe beam accumulated inside the plasma is presumed to be radially symmetric, it is possible to calculate the radial profile of the electron density representing the three dimensional distribution. A typical interferogram and the corresponding electron density are depicted in Figure 5.3.

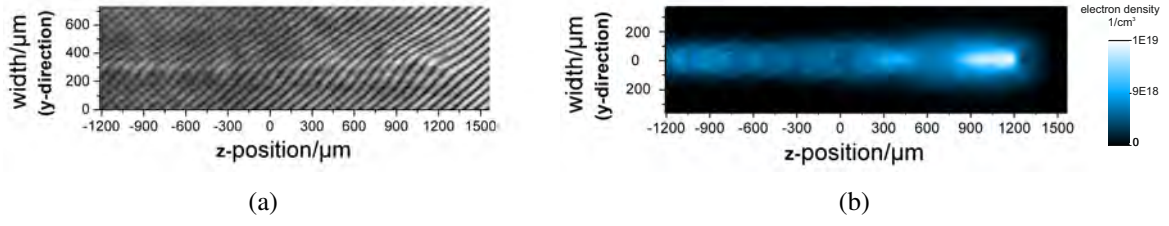


Figure 5.3: The interferogram in (a) contains the phase of the probe pulse. Assuming radially symmetric data the radial profile of the electron density (b) can be calculated from the interferogram. The middle of the gas nozzle with a 3 mm diameter is situated at position = 0.

The increasing laser intensity at the pulse front originating from the spatial intensity profile of the pulse causes an electron density gradient in laser direction. The electron density gradient

$$\frac{dn_e}{dz} \approx \frac{n_{e,\max}}{\Delta L} \quad (5.1)$$

can be approximated by the ratio of the maximal electron density  $n_{e,\max}$  and the rise length  $\Delta L$  which is the distance between maximal and zero electron density  $n_{e,\text{zero}}$ . By means of a horizontal lineout along the axis of symmetry, the peak electron density and the rise length can be determined. As Abel inversion relies on cylindrically symmetric data, the experimental data have to be symmetrized. In consequence, the algorithm fails on the axis of symmetry. As a compromise, the horizontal lineout (Figure 5.4(b)) shows the electron density close to the axis of symmetry.

The vertical lineout (Figure 5.4(b)) reveals the width of the ion front which can give evidence about the diameter of the pulse where the pulse intensity is about  $2 \times 10^{12} \text{ W/cm}^2$  which is the intensity threshold for tunnel ionization for helium.



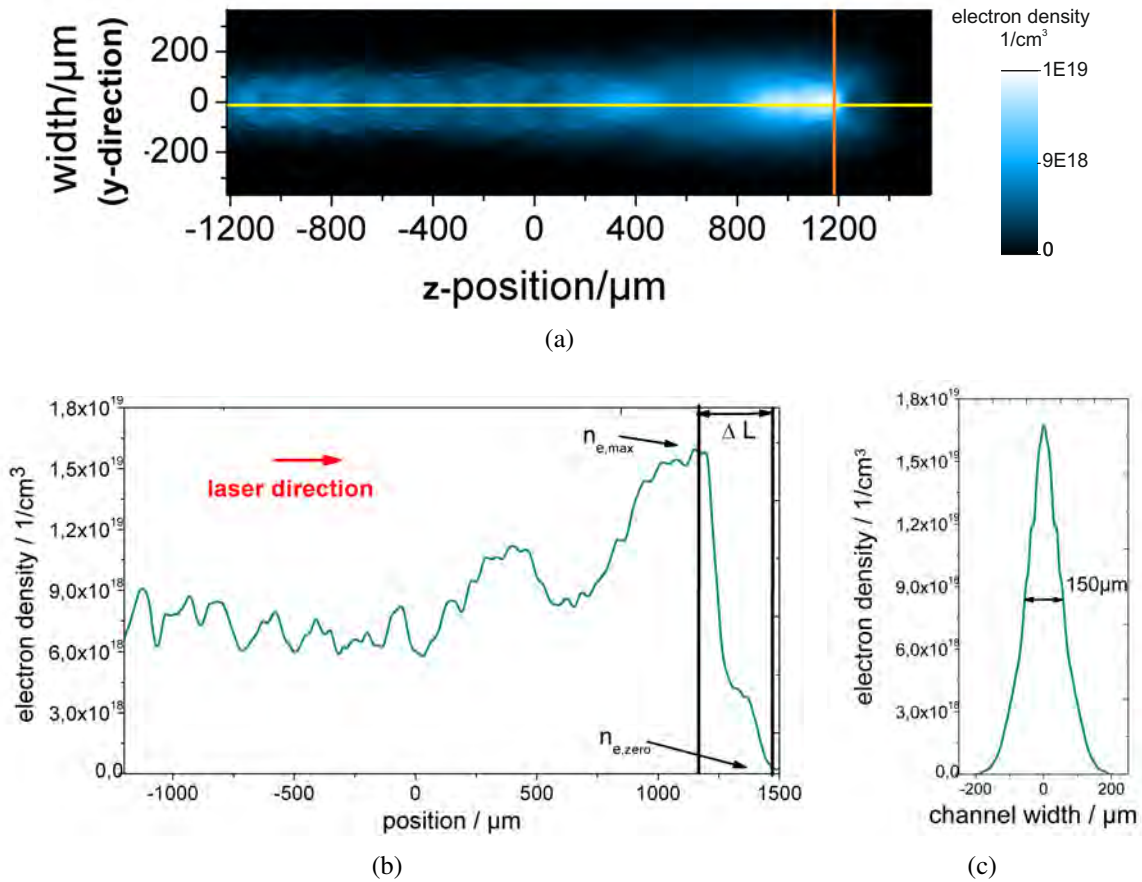


Figure 5.4: The electron density is studied taking lineouts of its radial profile. In the radial profile of the electron density (a) the positions of the horizontal (b) and vertical lineout (c) are marked yellow and orange, respectively. The middle of the gas nozzle with a 3 mm diameter is situated at position = 0.

The temporal shape of the main pulse was determined using third order autocorrelation. The autocorrelation trace was recorded in vacuum and therefore, it is not affected by nonlinear effects. However, in a plasma, the main pulse is modulated. As a result the leading edge of the main pulse inside a plasma is most probably steeper and the duration of the pulse is shorter. For this reason, an exact comparison of the autocorrelation trace and the horizontal lineout of the plasma density is not possible. Nevertheless, Figure 5.5 shows an overlap of the autocorrelation trace and the horizontal lineout of the plasma density. The distance between the intensities to singly and doubly ionize helium is in good agreement with the corresponding distance between maximal and half electron density in the horizontal lineout. It amounts to

about  $57\ \mu\text{m}$ , i.e. approximately 170 fs. The peak of the autocorrelation trace is situated  $35\ \mu\text{m}$  or 100 fs behind the intensity where helium is singly ionized. Considering pulse front steepening in the plasma, the peak of the modulated pulse probably arrives earlier than the peak of the pulse propagating in vacuum.

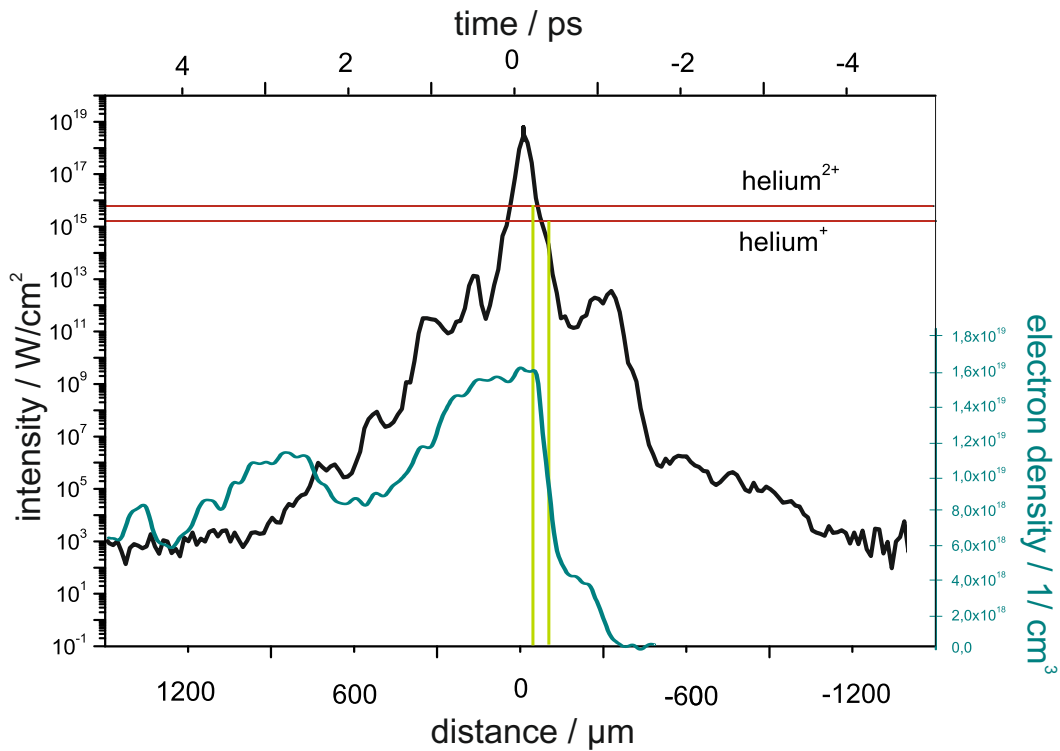


Figure 5.5: The third order autocorrelation trace of the main pulse (black) is overlapped with the horizontal lineout of the electron density (blue). The threshold intensity to singly and doubly ionize helium via over the barrier ionization are marked (red lines). The green lines mark the position of the maximal and the half electron density.

### 5.1.1 Accuracy of Optical Plasma Probing

Different effects influence the phase of the probe beam accumulated during its passage through the plasma. By means of theoretical simulations, the phase of the probe beam and the calculated electron density are compared for different probing conditions. Starting with an ideal probing situation, subsequently, three effects are discussed. These three effects are caused by probing at an angle, the finite duration of the probe pulse and the propagation of the main beam. Finally, these effects are combined to estimate the difference between ideal and real probing.

The simulations were realized using Labview. A radially symmetric three dimensional electron density distribution was generated. The image scale in the experiment as well as in the simulation amounts to  $2.7 \mu\text{m}/\text{px}$ . As the radial profile of the measured electron density (Figure 5.4(b)) the simulated density (Figure 5.6(a)) exhibits a density peak at the front. In the experiment and in the simulation a probe pulse with a duration of about 200 fs, corresponding to a longitudinal dimension of approximately  $67 \mu\text{m}$ , was used. To investigate the resolution due to the different effects, the magnitude of the profile is modulated sinusoidally with a wavelength of  $\lambda = 80 \mu\text{m}$ . In the horizontal lineout (Figure 5.6(b)) the peak and the modulation are clearly visible. A channel width of  $112 \mu\text{m}$  can be read from the vertical lineout (Figure 5.6(c)).

In the following, the phase of the probe beam has been calculated by accumulating the electron density according equation 4.5, i.e. all the single planes have been summarized along the propagation direction of the probe beam. The simulation is explained more thoroughly in appendix C.

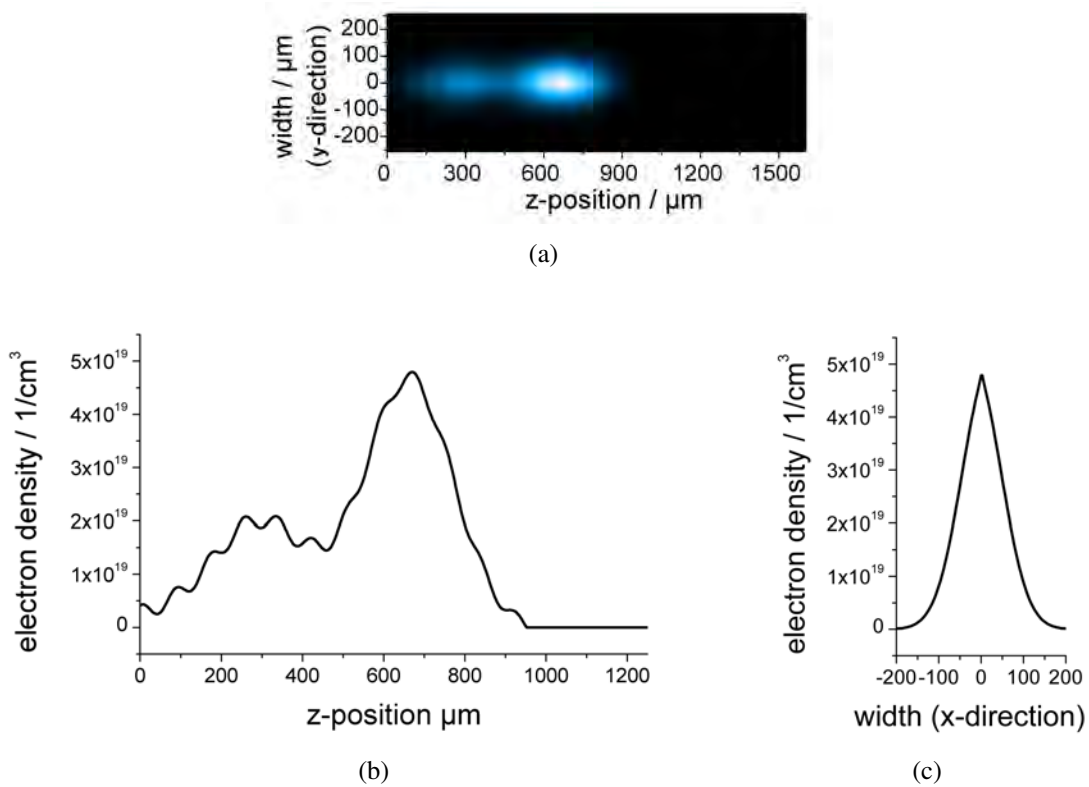


Figure 5.6: Simulation of the radial profile of the electron density (a) as well as the horizontal (b) and vertical lineout (c).

### Ideal Probing

The infinitely short probe pulse propagates through the stationary plasma perpendicularly to the propagation direction of the main beam. The phase of the probe beam accumulated in a plane  $y=\text{constant}$  is depicted in Figure 5.7. The electron density (Figure 5.6(a)) as well as phase shift of the probe beam (Figure 5.7) accumulated in the plasma are radially symmetric. Ideal probing reveals the exact distribution of the electron density.

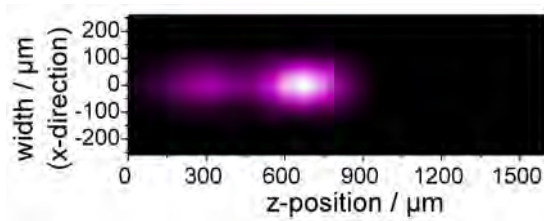


Figure 5.7: Phase in a plane  $y=\text{constant}$  if the plasma is probed at ideal conditions.

### Temporal Effects

A pulse has a finite duration  $\tau$ . Hence, one position in space is probed for a time identical to this duration. During this time, the channel is shifted by  $\Delta x = \tau v_g$  as the pulse propagates with its group velocity  $v_g$ . In consequence, the ionized area is the longer and the resolution the smaller the longer the pulse. In this measurement campaign, the electron density was measured interferometrically. This requires not only spatial but also temporal coherence. Therefore, the shorter the pulse, the smaller the interference pattern and thus, the area that contains the phase information (see section 3.2.1). In a simulation, the finite duration of a probe beam can be accounted for by averaging the images of the shifting plasma (Figure 5.8).

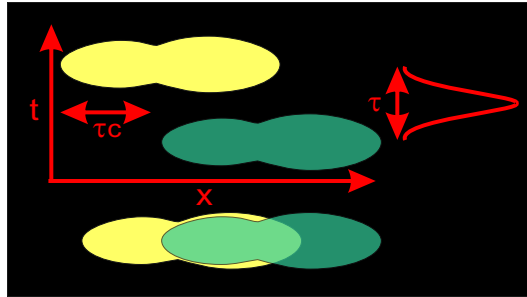


Figure 5.8: Scheme on temporal effects.

For a probe pulse with a duration of 200fs the length of the plasma is enhanced by about 67  $\mu\text{m}$ . Accordingly, a structure to be resolved clearly, has to be larger than 67  $\mu\text{m}$ . For an image scale of 2.67  $\mu\text{m}/\text{px}$  25 pictures subsequently shifted by one pixel in laser direction relative to each other have to be included in the calculation. Averaging over these pictures does not affect the radial symmetry of the phase of the probe beam (Figure 5.9(c)). The measured length of the channel (Figure 5.9(d)) is longer by  $\tau c$ . For this effect, the electron density is strongly smoothed due to the phase averaging in x-direction,.

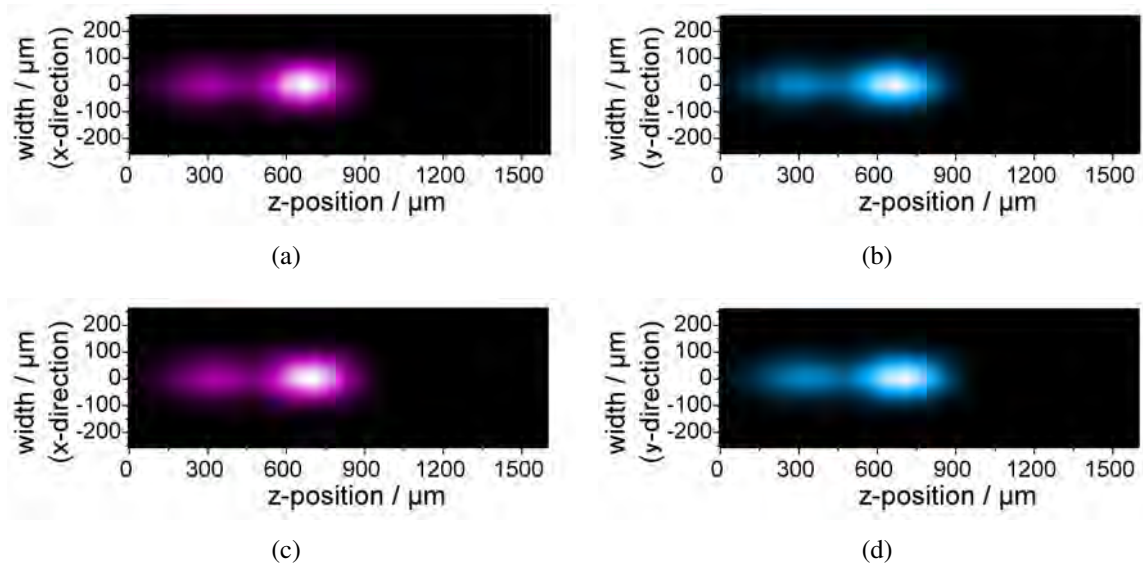


Figure 5.9: Phase (a) and electron density (b) in a plane  $y=\text{constant}$  for ideal probing compared to the phase (c) and electron density (d) calculated if a finite duration of the probe pulse is considered.

The horizontal lineout (Figure 5.10(a)) shows a shift in laser direction. Furthermore, the sinusoidal modulation has almost vanished. The amplitude of the electron density is slightly lower compared to ideal probing (figure 5.10(b)).

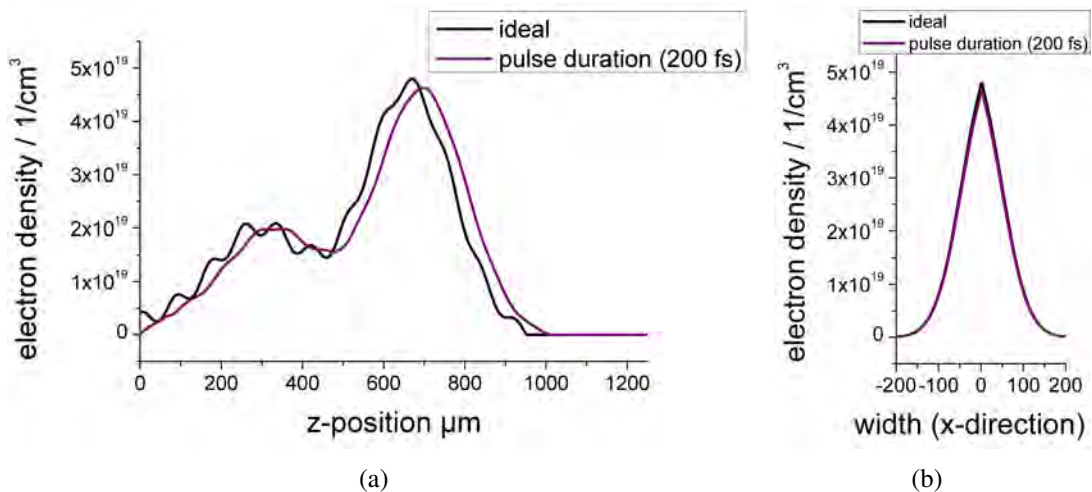


Figure 5.10: Horizontal (a) and vertical lineout (b) of the ideally probed plasma compared to the lineouts of the plasma probed with a finite probe pulse.

### Propagation Effects

While the probe beam propagates through the plasma, simultaneously, the main pulse is propagating in perpendicular direction, i.e., the electron density distribution is not stationary and the probe beam samples the electron density during the time the plasma is evolving. In a simple model each plane  $y=\text{constant}$  is shifted by the same distance the main pulse passes during that time. Thus, the probe beam experiences a skewed electron density distribution (Figure 5.11).

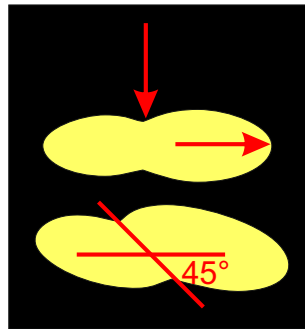


Figure 5.11: Scheme on propagation effects.

For that reason, the position of the plasma is shifted on the camera in laser direction depending on the shape of the ionization front. An averaged lengthening factor can be estimated by  $1/\cos(45^\circ)$  (Figure 5.12(d)) and in this regard, the electron density is lower by a factor of  $\cos(45^\circ)$ . Note, that this factor does not include the dependency on the actual shape of the electron density and can only be considered as an orientation.

As main and probe pulse propagate with the same velocity, for the probe pulse the plasma is skewed by  $45^\circ$  in laser direction. Thus, the sinusoidal modulation is rotated by  $45^\circ$  and the phase (Figure 5.12(c)) is not radially symmetric. Hence, the image of the electron density is blurred and the sinusoidal modulation not recognizable.

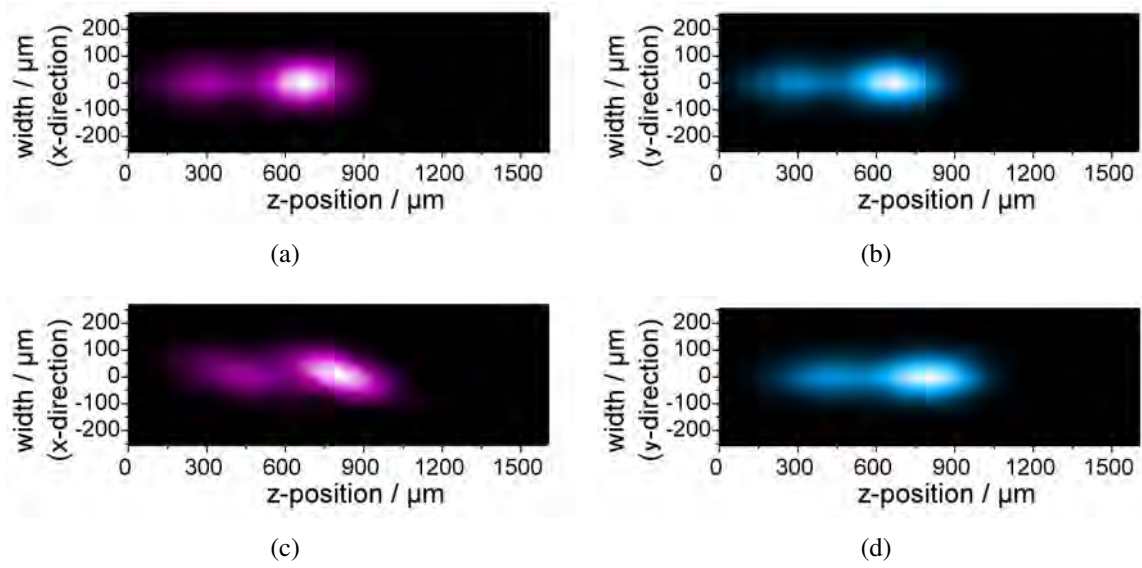


Figure 5.12: Real phase (a) and electron density (b) in a plane  $y=\text{constant}$  compared to the phase (c) and electron density (d) considering a propagating main pulse

The propagation effect has a stronger influence on the shape of the measured electron density than the temporal effect. The shift in laser direction is larger and no sinusoidal modulation is visible (Figure 5.13(a)). The vertical lineout clearly shows that the maximal electron density measured is even lower.

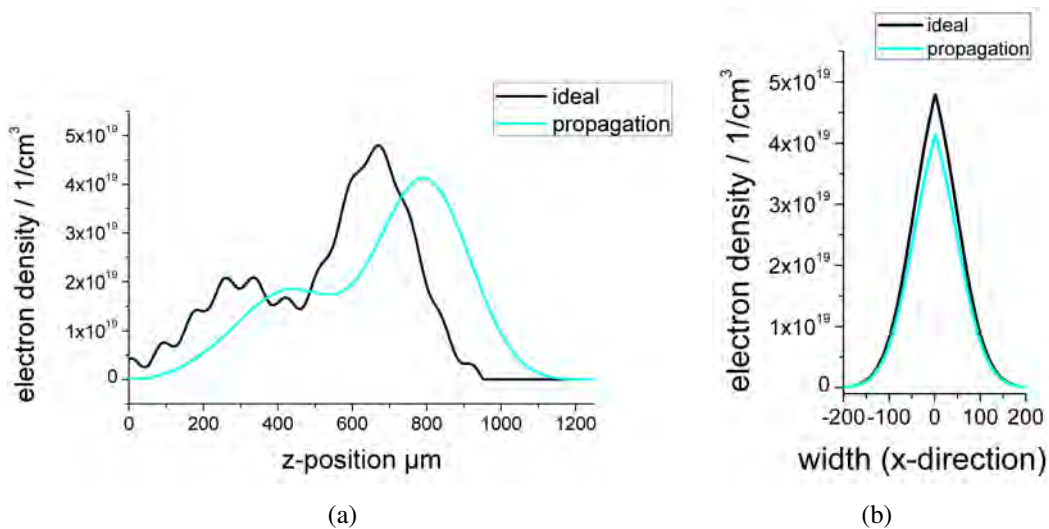


Figure 5.13: Horizontal (a) and vertical lineout (b) of the ideally probed plasma compared to the lineouts of the plasma probed considering a propagating main pulse.



### Angular Effects

Due to spatial restrictions in the target chamber, the plasma could not be probed perpendicular to the main beam direction. In this case, the probe beam passes the plasma at an angle  $\alpha$ . This angle describes the deviation of the angle between main and probe beam from  $90^\circ$ . Figure 5.14 shows a scheme on probing at an angle. Consulting this scheme, the real electron density as well as the length of the ionized area can be estimated from the measured ones. The probe beam experiences a shorter ionized area in conjunction with a stronger phase shift according to its longer way through the plasma. When a plasma of the length  $l$  is probed at an angle  $\alpha$ , the probed length  $l'$  is smaller by a factor  $\cos(\alpha)$ , i.e

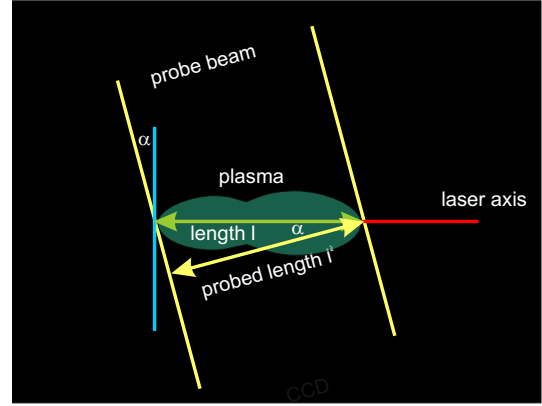


Figure 5.14: Scheme on angular effects.

$$l = \frac{l'}{\cos(\alpha)}. \quad (5.2)$$

Accordingly, the plasma density  $n_e$  can be estimated by

$$n_e = n'_e \cos(\alpha). \quad (5.3)$$

For an angle of  $15^\circ$  the factor  $\cos(\alpha)$  amounts to about 0.97 so that only small changes are expected. Figure 5.15 depicts the phase of the probe beam in a plane  $y=\text{constant}$  and the calculated radial profile of the electron density.

If the probe beam passes the plasma at an angle, it experiences the sinusoidal modulation as rotated by that angle (Figure 5.15(c)). Hence, the phase of the probe beam is not radial symmetric and the calculated electron density distribution (Figure 5.15(d)) is slightly smoothed.

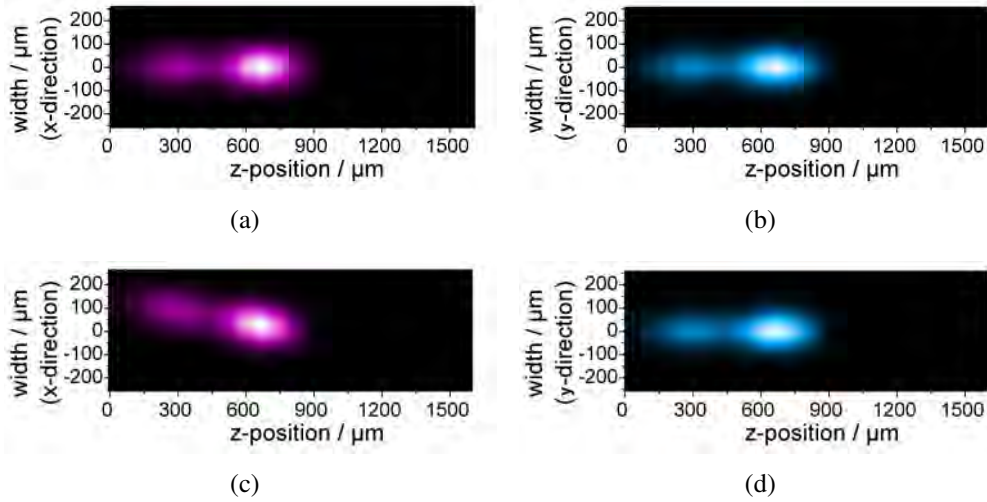


Figure 5.15: Phase in a plane  $y=\text{constant}$  (a) and radial profile of the electron density (b) for ideal probing compared to the phase (c) and electron density (d) extracted if the plasma is probed at an angle  $\alpha = 15^\circ$ .

Horizontal (Figure 5.16(a)) and vertical lineout Figure 5.16(b)) show that the discrepancy between ideal probing and probing at  $\alpha = 15^\circ$  is negligible. The position on the camera, the sinusoidal modulation as well as the amplitude are preserved. Note that the resolution of the sinusoidal modulation depends on the wavelength for this effect as well. A modulation with a wavelength of about  $30\mu\text{m}$  would have vanished.

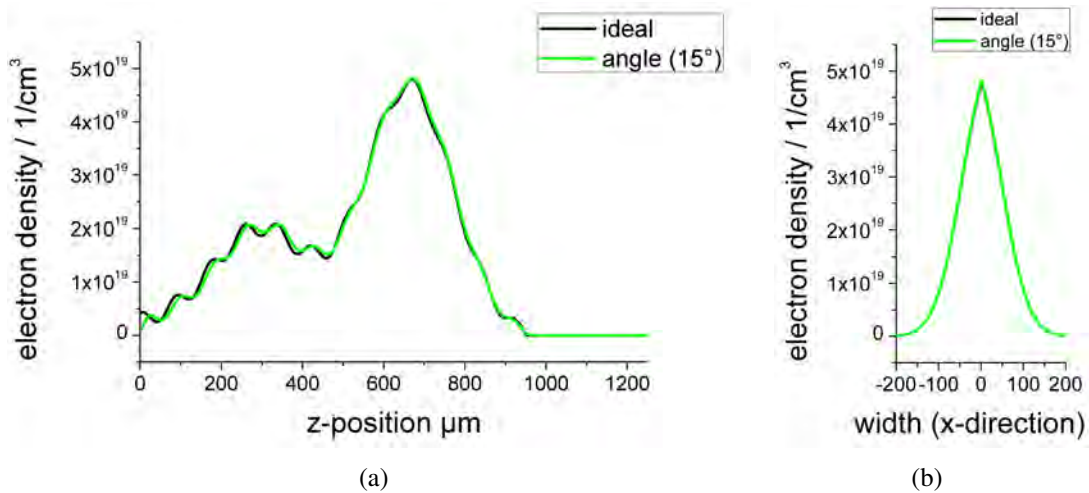


Figure 5.16: Horizontal (a) and vertical lineout (b) of the ideally probed plasma compared to the lineouts of the electron density measured at an angle.

### Combined Effects

Considering all three effects simultaneously results in a strong deformation of the phase of the probe beam accumulated in the planes  $y_i = \text{constant}$ . Similar to the propagation effect, in this case one can identify no sinusoidal modulation in the electron density distribution (Figure 5.17).

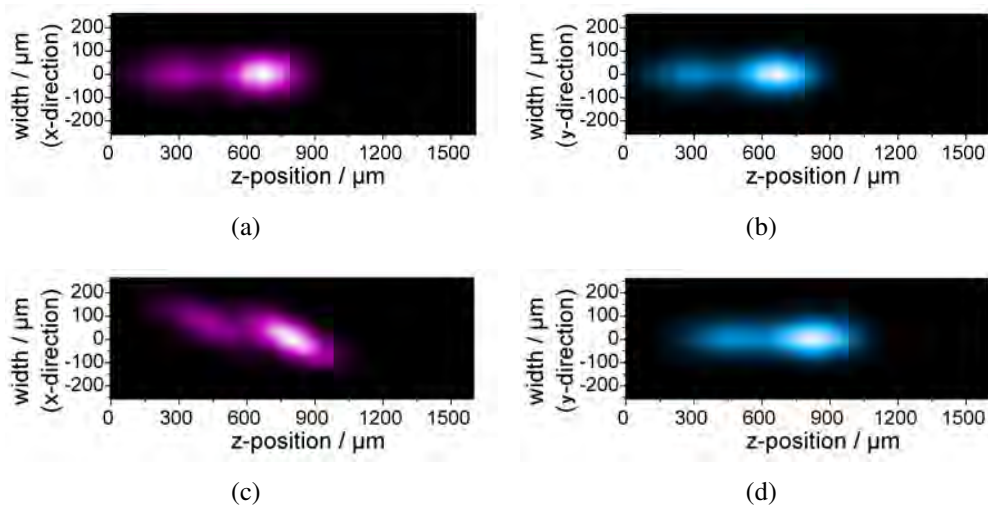


Figure 5.17: Phase (a) and radial profile of the electron density (b) in a plane  $y = \text{constant}$  for ideal probing compared to the phase (c) and radial profile of the electron density (d) considering all effects discussed.

The lineouts (Figure 5.18) show that the measured electron density is strongly influenced by the propagation effect.

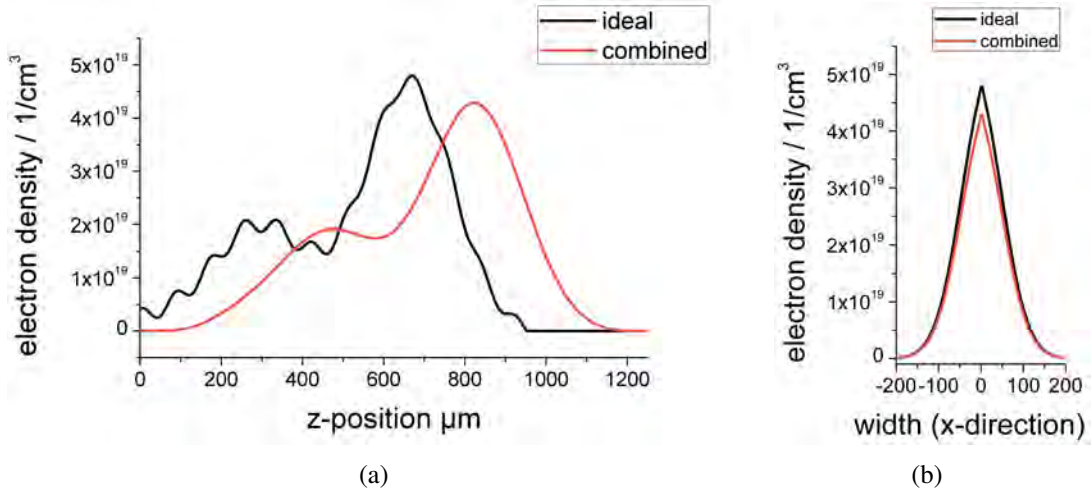


Figure 5.18: Horizontal (a) and vertical (b) lineout of the ideally probed plasma compared to the lineouts of the plasma probed at real conditions.

For the combined effects the length of the channel can be approximated to

$$l = l' \frac{\cos(15^\circ)}{\cos(45^\circ)} = 1.37 \cdot l' \quad (5.4)$$

and the electron density to

$$n_e = n_e' \frac{\cos(45^\circ)}{\cos(15^\circ)} = 0.73 \cdot n_e'. \quad (5.5)$$

Figure 5.19 shows the lineouts for the different probing conditions in comparison.

Treated as septate effects, the duration of the probe pulse (200 fs) and a probing angle of  $15^\circ$  only slightly influence the shape of the distribution of the plasma density. While the sinusoidal modulation of the plasma density with a wavelength of  $80 \mu\text{m}$  is preserved very well for probing at  $\alpha = 15^\circ$ , it is strongly damped considering a probe pulse duration of 200 fs. The simultaneous propagation of main and probe pulse leads to a shift in position of the plasma on the camera and the overall structure of the horizontal lineout is slightly obliterated. The FWHM of the width of the channel is roughly the same for all the effects considered separately as well as combined. If the effects discussed occur contemporaneously, the strong influence of the propagation of the main beam on the amplitude of the electron density is counteracted marginally.

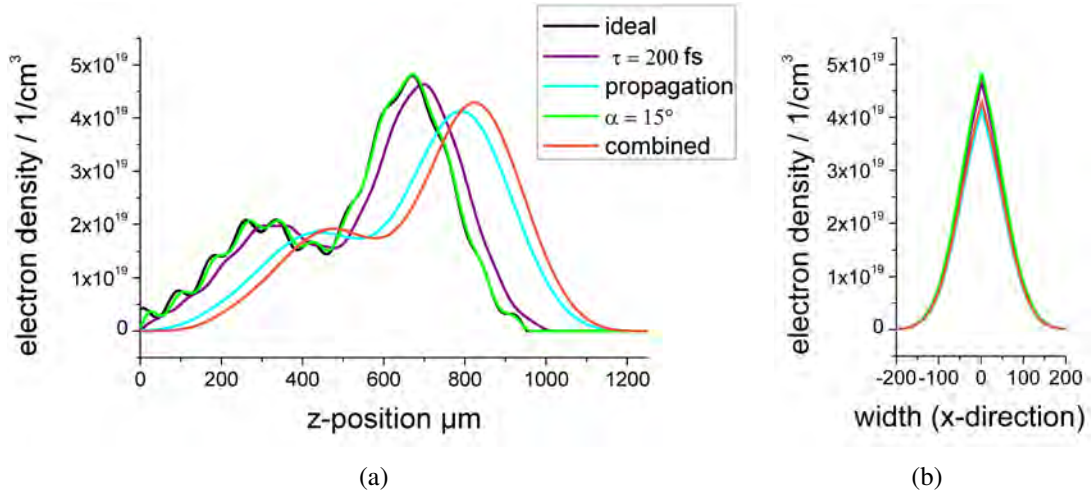


Figure 5.19: Horizontal and vertical lineouts of the plasma density probed a different conditions: finite duration  $\tau$  of the probe pulse, simultaneous propagation of main and probe pulse and probing at an angle  $\alpha$ . The legend in (a) is also valid for (b).

Comparing the horizontal lineouts of the ideally probed plasma density and the plasma density comprising all three effects a transformation factor  $f_{\text{trans}}$  can be found

$$f_{\text{trans}} = \frac{n_e(\mathbf{r})}{n'_e(\mathbf{r})}. \quad (5.6)$$

This factor in the range of 50-800  $\mu\text{m}$  and the corresponding densities are depicted in Figure 5.20. The transformation factor varies between about 0.75 and 1.25, i.e, it is lower than the estimated factor of  $\cos(15^\circ)/\cos(45^\circ) = 1.37$ . However, the deviation between the two lineouts amounts to  $\pm 25\%$  and therefore, it is in the range of the expected deviation of 20% originating from Abel inversion. Note that the temporal effect has not been considered in equations 5.4 and 5.5. Furthermore, it is only an approximation of the dimension of the inaccuracy as the dependency of the transformation factor on the shape of the actual plasma density has not been considered.

All the effects discussed lead to systematic differences between actual and measured electron density distribution. Moreover, the shape of the electron density distribution is preserved. Therefore, it is possible to investigate the acceleration process.

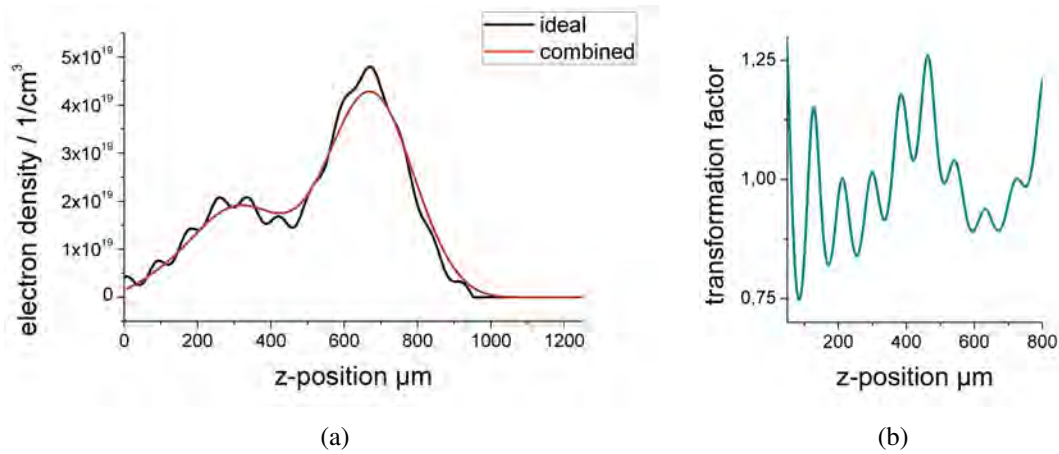


Figure 5.20: The horizontal lineout of the plasma probed considering all three effects is shifted along the  $z$ -axis so that its peak has the same  $z$ -position as the peak of the horizontal lineout of the ideally probed plasma (a). Calculating the ratio  $n_e:n'_e$  the transformation factor is yielded and visualized in the range of 50-800  $\mu\text{m}$  (b).

## 5.2 Pointing and Divergence of the Electron Beam

Employing a movable aiming screen, the pointing of the electron beam can be determined. In Figure 5.21(a) 20 shots onto an aiming screen are averaged and additionally, the centroid of each of the shots is marked. The pointing of the electron bunches depends on parameters such as the pointing of the laser pulse, the injection of the electrons into the wakefield and fluctuations of the gas density. Figure 5.21(a) illustrates that the pointing varies over more than 100 mrad in  $x$ - as well as in  $y$ -direction. Figure 5.21(b) reveals information on the divergence of an electron beam. The width of the plasma channel is in the order of few  $\mu\text{m}$  and the FWHM width at the aiming screen in a distance of 330 mm from the target amounts to 2.5 mm in  $x$ -direction which is the plane of dispersion. Assuming a channel width of 10  $\mu\text{m}$  the divergence of the electron bunch is 75 mrad. The divergence of the electrons strongly depends on the focusing effect of the wakefield on the electrons (section 2.2.5).

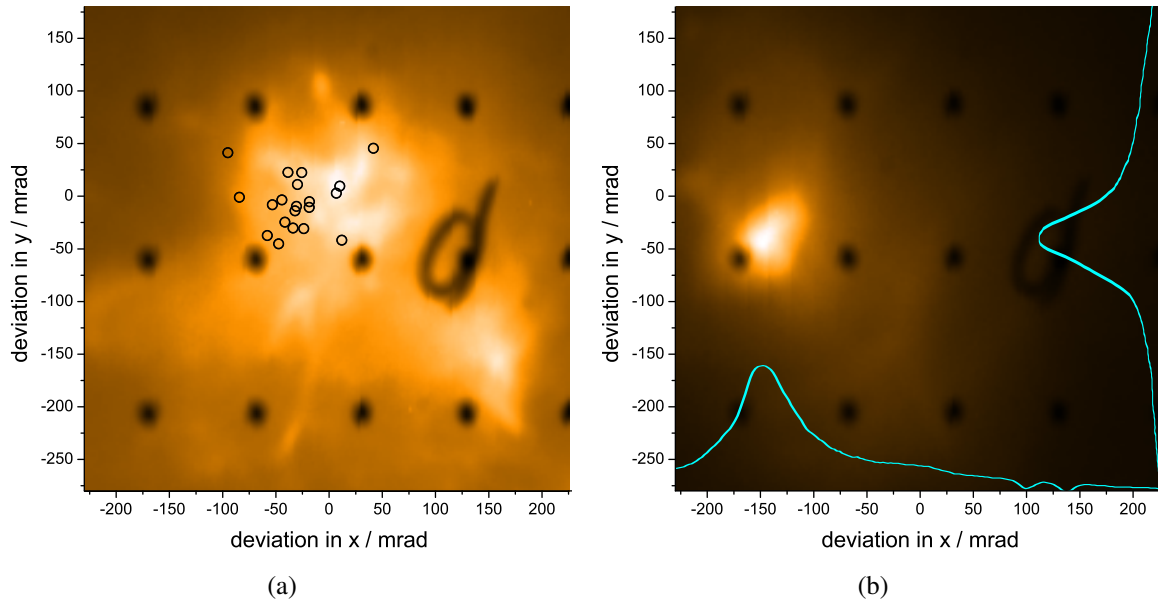


Figure 5.21: The pointing of 20 shots onto the aiming screen is averaged and depicted in (a). The centroid of the average is situated at zero deviation in both directions. Moreover, the centroid of each of the shots is marked. In (b) lineouts through the centroid of an electron pulse on the aiming screen are depicted. The divergence of the electron bunch in  $x$ -direction amounts to about 75 mrad.

### 5.3 Electron Spectra

The following electron spectrum has been recorded simultaneously to the electron density distribution presented in section 5.1. *Low* (10 – 55 MeV) and *high energy* (60 – 240 MeV) electrons were detected with separate screens. Due to different aperture settings of the CCD cameras, the images of low and high energy screen had to be normalized to each other. Figure 5.22(a) shows the images of low and high energy screen. The low energy screen on the left hand side of the image shows an intensity distribution mainly caused by single photon events that can be connected to  $\gamma$ -rays due to Bremsstrahlung. However, at the high energy screen, besides the single photon events, an electron bunch has been observed.

The energy of the electrons detected at the screens increases in  $z$ -direction. One column of pixels at a constant value of  $z$  represents the same electron energy. Creating a histogram, the image can be transformed into a graph of the intensity of the phosphorescence in dependence on the electron energy (Figure 5.22(b)).



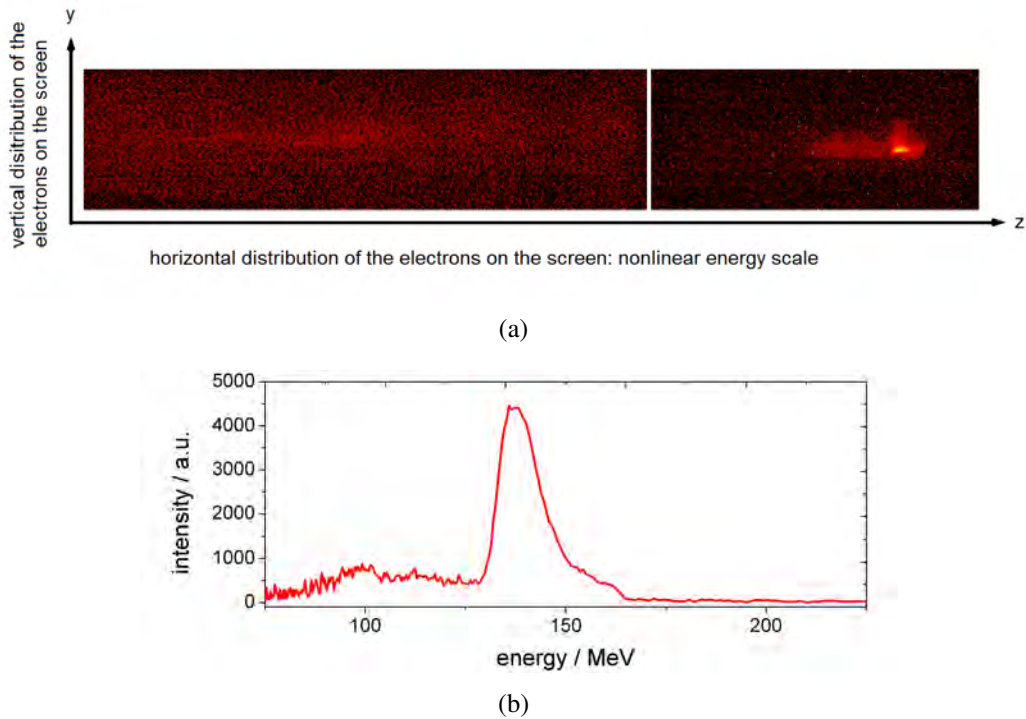


Figure 5.22: The electron energy is measured at phosphorescent screens and depicted with CCD cameras (a). By means of the histogram (b) the peak energy can be determined to  $(137 \pm 3)$  MeV and the FWHM to 12 MeV.

Thereby, the nonlinear dependency of the energy on the position on the screens is calibrated employing the measured magnetic field<sup>40</sup> of the spectrometer. At about  $137 \pm 3$  MeV, the peak of the spectrum with a FWHM of 12 MeV is situated. The inaccuracy of the electron energy is given by the magnetic field inside the magnet yoke and the maximal angle of divergence of the electron bunch determined by the slit at the entrance of the spectrometer which is situated in a distance of 1 m from the target. Owing to this 2 mm slit, electrons with a deviation of more than  $1 \text{ mrad}$ <sup>1</sup> from the laser axis in x-direction were not detected.

## 5.4 Correlations

In the underlying measurement campaign, more than 1000 shots into a He gas target have been recorded. In this scope, the gas pressure was varied to find an optimal electron density.

<sup>1</sup>Half opening angle.



For each pressure value chosen, the pointing and divergence of the electron beam has been recorded. Afterwards, the electron density has been probed at different times during the interaction and simultaneously, the electron energy has been measured. For more than 40% of the shots electrons have been detected in the spectrometer. Due to a 2 mm slit perpendicular to the plane of dispersion at the entrance of the spectrometer, it cannot be ruled out that fast electrons were generated even if no electrons were incident at the phosphorescent screens. For this reason, only shots where electrons have been detected in the spectrometer were included into the data evaluation process.

The main pulse was focused into the leading edge of the gas jet. At early times during the interaction, i.e., before the ionization front has reached the middle of the gas nozzle, the maximal electron density is comparably low and varies strongly. Presumably, in this region the peak intensity of the laser is maximal and is kept over several Rayleigh lengths owing to self focusing. It can be assumed that a fraction of the free electrons is expelled into regions of low laser intensity and the plasma wave becomes nonlinear, breaks and injects electrons into the wakefield.

When the ionization front has passed the middle of the gas nozzle, the maximal electron density is higher and varies less. Here, the laser pulse might become defocused so that the ponderomotive force pushes less electrons away from the laser axis causing a maximal electron density. The electron density in dependence on the position of the ionization front, or rather the time during the interaction, is illustrated in Figure 5.23(a). The width of the electron density distribution (Figure 5.23(b)) increases and varies more strongly the later the time during the interaction. An increasing channel width might be explained by an increasing beam diameter due to defocusing of the regions of the laser pulse where the angle of self focusing is not sufficient to compensate the angle of diffraction. The more laser energy is deposited in the plasma channel caused by the self focused part of the laser pulse, close to the axis of symmetry, the less energy is available for ionization in the regions outside the plasma channel. Laser wakefield acceleration is a strongly nonlinear process. Hence, a small change of parameters at the beginning of the process causes a large difference of the result at the end of the interaction. Therefore, strongly varying parameters at late times during the interaction have been expected.

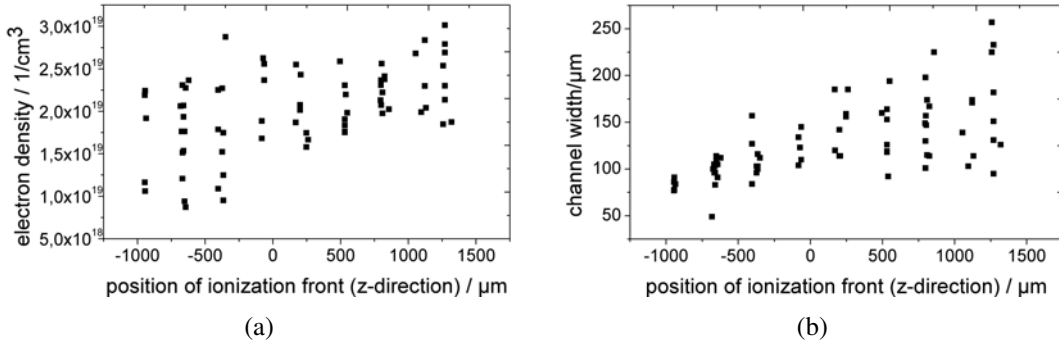


Figure 5.23: Electron density and width of its distribution for different times during the interaction. The further the ionization front has propagated the later during the interaction the plasma was probed. The middle of the gas nozzle with a 3 mm diameter is situated at position = 0.

Following the approximation of the electron density gradient

$$\frac{dn_e}{dz} \approx \frac{n_{e,max}}{\Delta L} \quad (5.7)$$

it increases with increasing electron density and decreasing rise length. The gradient in dependence on the maximal electron density and the rise length is illustrated in Figure 5.24.

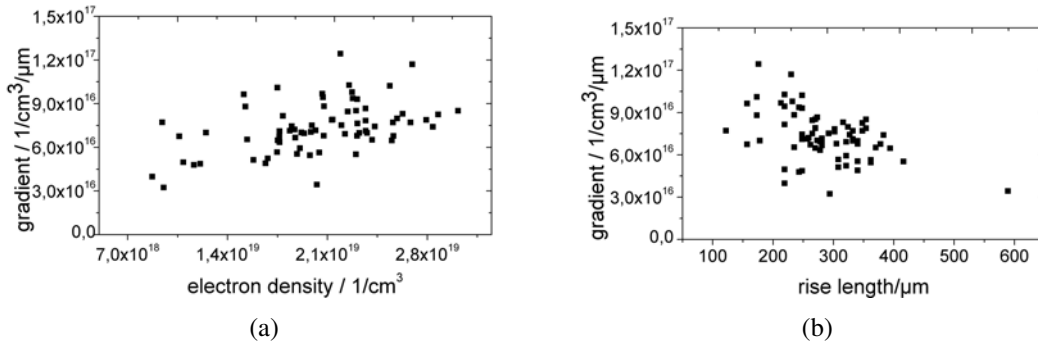


Figure 5.24: Gradient in dependence on the plasma density and the rise length.

For the latest times during the interaction the dependency of electron energy on the electron density gradient has been determined. The electron energy is maximized for small widths and high electron density gradients (Figure 5.25).

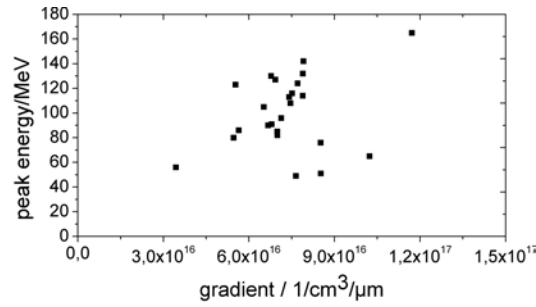


Figure 5.25: Electron peak energy in dependence on the electron density gradient.

Considering that the electron density gradient is related to the shape of the main pulse (Figure 5.5), the relation between electron density gradient and energy is supported by previous experiments. Leemans et al. investigated that the temporal shape of the laser pulse influences the electron acceleration process. A steep rising edge and a slowly trailing one benefits the acceleration process while in the reverse situation the yield of the process is decreased<sup>46</sup>.

## 6 Summary

Within the scope of this diploma thesis, a new probe beam for the JETI-laser system has been set up. A high temporal resolution is desired in order to investigate processes on short time scales as thorough as possible. Therefore, dispersive effects have been minimized owing to the employment of a mirror instead of a lens telescope. Furthermore, the pulse duration can be measured using the integrated single shot autocorrelator. Hence, the possibility to install chirped mirrors to reduce the pulse duration to its minimum limited by higher order dispersion is given. Near and far field diagnostics allow the observation of possible beam displacements, i.e, the probe beam can be adjusted to an accuracy in the sub-mrad regime. In combination with the motorized mirrors of the delay stage, the displacement arising from the movement of this delay stage can be compensated remotely with a PC.

The accuracy of optical probing has been analyzed via theoretical simulations. In these simulations, the pulse duration of the probe pulse, the simultaneous propagation of main and probe pulse and probing at an angle have been considered. The simultaneous propagation of main and probe beam most strongly affects the measured electron density. Next to a shift of the maximal electron density, a sinusoidal modulation with a wavelength larger than the longitudinal dimension of the probe pulse cannot be resolved and the electron density has a smaller amplitude. Combining these three effects, the propagation effect is slightly counteracted concerning the amplitude of the electron density. As the overall shape of the electron density is preserved, it is possible to investigate the acceleration process.

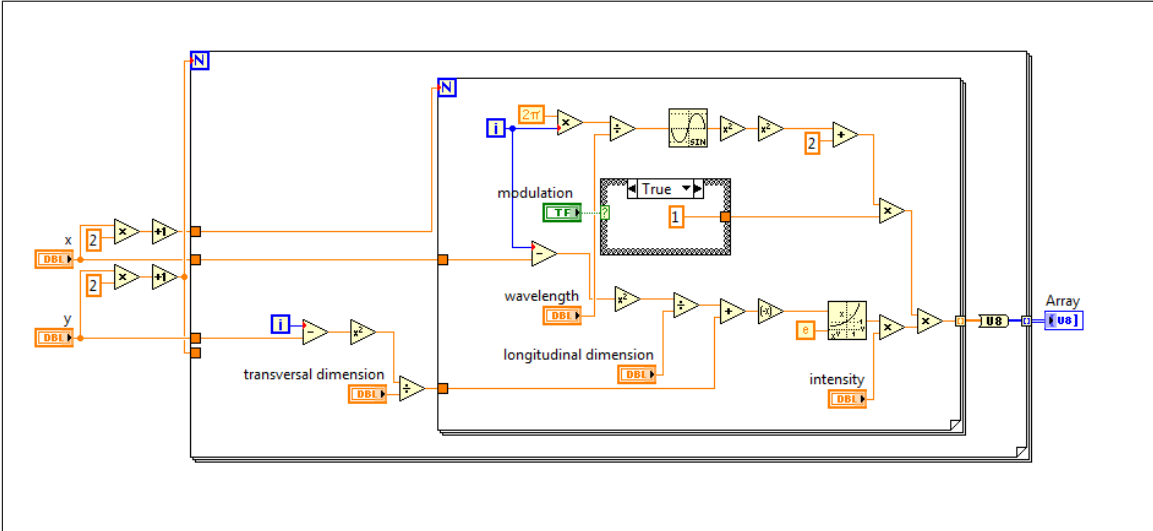
In an experiment in the field of laser wakefield acceleration, the probe beam has been applied successfully. Thereby, the plasma was examined. The electron densities of a plasma originating from a helium gas jet have been calculated. Electron density and energy have been measured simultaneously. Therefore, it was possible to investigate the correlation of the corresponding results. As a slit with a width of 2 mm perpendicular to the plane of dispersion was situated at the entrance of the electron spectrometer, not for every shot electrons could be

detected at the phosphorescent screens although highly energetic electrons, i.e. electrons with energies between 180 and 190 MeV, might have been generated. For this reason, only the data of shots for which the electron energy could be quantified have been included in the data evaluation process. It could be observed that if high electron density gradients in laser direction were present at late times during the interaction, high electron energies were achieved.

Laser wakefield acceleration is a highly nonlinear process. To stabilize the parameters of the electron bunches, a thorough investigation of the process is required. Temporal and spatial resolution play an important role for optical probing. It is possible to measure not only the electron density but also gain a direct insight into the acceleration process. The magnetic field structures have been studied by M. Kaluza et al.<sup>47</sup> with an 80 fs probe pulse and a spatial resolution of 10 and 30  $\mu\text{m}$  in the transverse and laser direction, respectively. Employing the same method but a probe pulse with a duration of 8 fs and a spatial resolution of 2  $\mu\text{m}$  A. Buck, M. Nicolai et al.<sup>48</sup> directly investigated the length of an electron bunch to  $6 \pm 2$  fs. Additionally, the plasma wave could be imaged. In further measurements at the JETI-laser facility, the influence of the electron density gradient as well as the width of the ionized area will be investigated more thoroughly improving the temporal resolution. For small structures to be resolved, such as the plasma wave which is in the order of 10  $\mu\text{m}$ , corresponding to 30 fs, the probe pulse should have a duration of maximal 10 fs. To improve the temporal resolution of the JETI-probe pulse, its spectrum will be broadened applying a gas filled hollow fiber.

# Appendices

## A Labview-Program for pulse modulation in a Uniform Plasma Wave

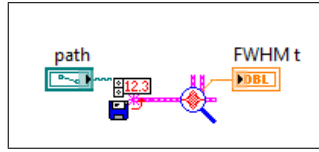


## B Calculation of the Pulse Duration

To calculate the pulse duration Lab2 was used. Fouriertransforming the spectrum gives the intensity of the pulse in dependence on the time

$$I(t) = \frac{1}{2\pi} \int_{-\infty}^{\infty} \exp\{-i\omega t\} d\omega.$$

The FWHM pulse duration can be obtained from that.



Labview-program to calculate the FWHM pulse duration for a given spectrum.

To account for the dispersive media in the beam path the phase

$$\Delta\phi(\omega) = \frac{\omega}{c}\eta(\omega)z \quad (.1)$$

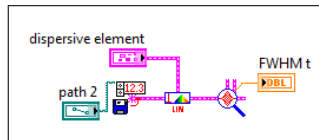
induced by the frequency dependent index of refraction is used. Taylor expansion yields  $\frac{1}{n!}\phi^{(n)}(\omega_0)$  for the material coefficients causing dispersion (see section 2.1.1). In Lab2 these are calculated using<sup>49</sup>

$$\phi^{(n)}|_{\omega_0} = \frac{z}{c} \left[ n \frac{\partial^{(n-1)}\eta}{\partial\omega} |_{\omega_0} + \omega_0 \frac{\partial^{(n)}\eta}{\partial\omega} |_{\omega_0} \right]. \quad (.2)$$

By means of the Sellmeier equation

$$\eta(\lambda)^2 = 1 + \sum_j \frac{B_j \lambda^2}{\lambda^2 - \lambda_j^2} \quad (.3)$$

where  $\lambda_j$  and  $B_j$  are material specific constants the refractive index is calculated.



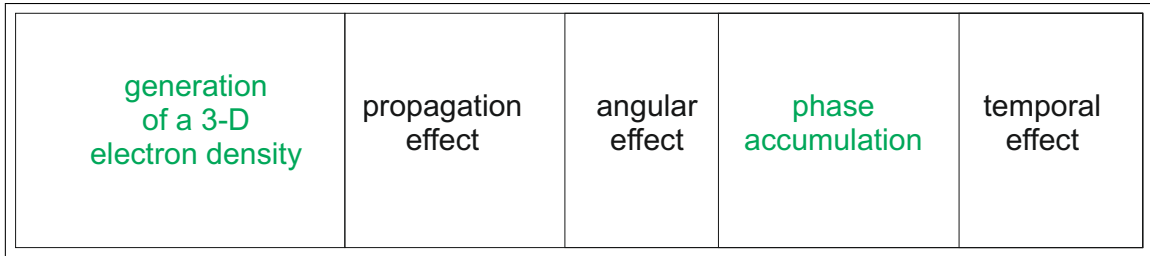
Labview-program to calculate the FWHM pulse duration for a spectrum affected by dispersion.

## C Labview-Program to evaluate the accuracy of optical plasma probing

To investigate the accuracy of optical plasma probing a three-dimensional radially symmetric electron density was generated. Subsequently, the propagation effect and the angular effect can be simulated optionally while phase accumulation is mandatory. Finally, the duration of

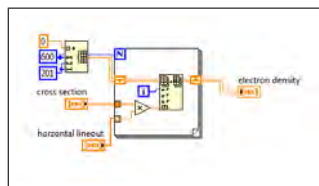
## CHAPTER 6. SUMMARY

the probe pulse can be included in the calculation. The effects can be examined separately or in combination. Nevertheless, the order of the processes is defined as depicted in the following Figure.



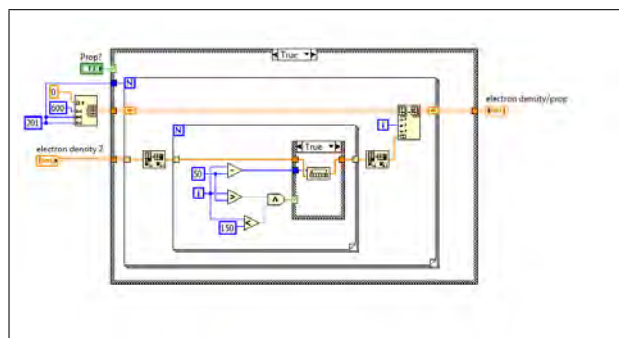
Scheme of the simulation to evaluate the accuracy of optical plasma probing. The mandatory steps are marked green and the optional ones black.

Multiplying a two-dimensional Gaussian distribution with a modulated z-profile a three-dimensional electron density was generated:



Generation of a radially symmetric three-dimensional electron density.

To simulate the simultaneous propagation of main and probe beam, the inner part of the planes  $y_i$  has been skewed by shifting the lines  $x_{jk}$  in z-direction. As only the inner part of the image comprises the plasma only the lines for  $j=51\dots150$  are shifted by  $k=j-50$  px.

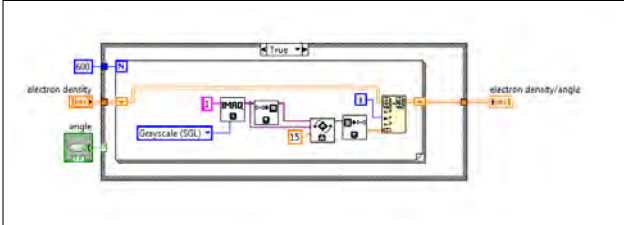


Simulation of the propagation effect.



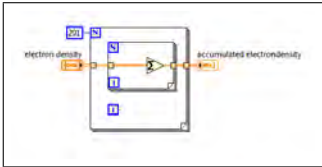
CHAPTER 6. SUMMARY

The rotation of the plasma is realized by rotating each plane  $z_i$  by  $15^\circ$ . Up to this junction the output is three-dimensional.



Simulation of the angular effect.

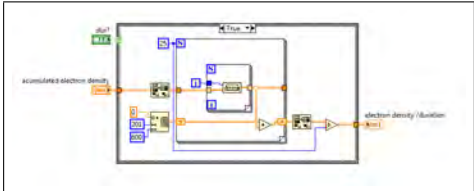
Summarizing along each array  $y_{i,j}=\text{constant}$  the electron density is accumulated, i.e. the two-dimensional accumulated electron density distribution is generated.



Phase accumulation.

If the accumulated electron density is averaged over  $n$  pictures consecutively shifted by one pixel in propagation direction the finite duration of the probe pulse can be accounted for.  $n$  depends on the image scale and the pulse duration  $\tau$

$$n = \frac{\tau}{\text{image scale}}$$



Simulation of the temporal effect.

# Bibliography

- [1] W. P. Leemans, B. Nagler, A. J. Gonsalves, C. Toth, K. Nakamura, C. G. R. Geddes, E. Esarey, C. B. Schroeder and S. M. Hooker: *GeV electron beams from a centimetre-scale accelerator*, Nat Phys **2** (10), 2006
- [2] T. Tajima and J. M. Dawson: *Laser Electron Accelerator*, Physical Review Letters **43** (4), 1979
- [3] A. Pukhov and J. Meyer-ter Vehn: *Laser wake field acceleration: the highly non-linear broken-wave regime*, Applied Physics B-Lasers and Optics **74** (4-5), 2002
- [4] S. P. D. Mangles, C. D. Murphy, Z. Najmudin, A. G. R. Thomas, J. L. Collier, A. E. Dangor, E. J. Divall, P. S. Foster, J. G. Gallacher, C. J. Hooker, D. A. Jaroszynski, A. J. Langley, W. B. Mori, P. A. Norreys, F. S. Tsung, R. Viskup, B. R. Walton and K. Krushelnick: *Monoenergetic beams of relativistic electrons from intense laser-plasma interactions*, Nature **431** (7008), 2004
- [5] C. G. R. Geddes, C. Toth, J. van Tilborg, E. Esarey, C. B. Schroeder, D. Bruhwiler, C. Nieter, J. Cary and W. P. Leemans: *High-quality electron beams from a laser wakefield accelerator using plasma-channel guiding*, Nature **431** (7008), 2004
- [6] J. Faure, Y. Glinec, A. Pukhov, S. Kiselev, S. Gordienko, E. Lefebvre, J. P. Rousseau, F. Burgy and V. Malka: *A laser-plasma accelerator producing monoenergetic electron beams*, Nature **431** (7008), 2004
- [7] R. Benattar, C. Popovics and R. Sigel: *Polarized light interferometer for laser fusion studies*, Review of Scientific Instruments **50** (12), 1979
- [8] K.-U. Amthor: *Plasmadiagnose in Experimenten zur Wechselwirkung intensiver Laserpulse mit Materie*, Friedrich Schiller Universität Jena, Diploma thesis 2002

## Bibliography

---

- [9] W. Becker, F. Grasbon, R. Kopold, D. B. Milosevic, G. G. Paulus, H. Walther, B. Benjamin and W. Herbert: *Above-threshold ionization: From classical features to quantum effects*, Bd. Volume 48, Academic Press, 2002
- [10] H.-P. Schlenvoigt: *Synchrotron Radiation Sources driven by Laser-Plasma Accelerators*, Friedrich Schiller Universität Jena, Dissertation 2009
- [11] A. A. M. Wollenhaupt and T. Baumert: *Handbook of Lasers and Optics, Femtosecond Laser Pulses*, 2007
- [12] A. E. Siegman: *Lasers*, University Science Books 1986
- [13] J. D. Jackson: *Classical Electrodynamics*, John Wiley and Sons, Inc. 1962
- [14] D. Strickland and G. Mourou: *Compression of amplified chirped optical pulses*, Optics Communications **56** (3), 1985
- [15] Amplitude: *Handbook for high contrast frontend*
- [16] R. Trebino: *The Dilemma*, [http://frog.gatech.edu/Books/Ch01\\_%20FROG.pdf](http://frog.gatech.edu/Books/Ch01_%20FROG.pdf)
- [17] R. W. Boyd: *Nonlinear Optics*, Academic Press, Inc. 2008
- [18] F. Salin, P. Georges, G. Roger and A. Brun: *Single-shot measurement of a 52-fs pulse*, Appl. Opt. **26**, 1987
- [19] Y. Ishida, T. Yajima and A. Watanabe: *A simple monitoring system for single subpicosecond laser pulses using an SH spatial autocorrelation method and a CCD image sensor*, Optics Communications **56** (1), 1985
- [20] P. Simon, H. Gerhardt and S. Szatmari: *A SINGLE-SHOT AUTOCORRELATOR FOR UV FEMTOSECOND PULSES*, Measurement Science and Technology **1** (7), 1990
- [21] National Institute of Standards and Technology <http://physics.nist.gov/PhysRefData/Handbook/Tables/heliumtable1.htm>
- [22] L. V. Keldysh: *IONIZATION IN FIELD OF A STRONG ELECTROMAGNETIC WAVE*, Soviet Physics JETP-USSR **20** (5), 1965

## Bibliography

---

- [23] P. Gibbon: *Short pulse laser interactions with matter*, Imperial College Press 2005
- [24] S. Kneip: *Laser Plasma Accelerator and Wiggler*, Imperial College London, Dissertation 2010
- [25] S. P. D. Mangles: *Measurements of Relativistic Electrons from Intense Laser-Plasma Interactions*, Imperial College London, Dissertation 2005
- [26] F. F. Chen: *Introduction to Plasma Physics and Controlled Fusion*, Plenum Press 1984
- [27] J. A. Bittencourt: *Fundamentals of Plasma Physics*, Springer 2004
- [28] C. Widmann: *Laser-Wakefield-Beschleunigung am JETI*, Friedrich Schiller Universität Jena, Diploma thesis 2001
- [29] E. Esarey, A. Ting and P. Sprangle: *Frequency shifts induced in laser pulses by plasma waves*, Physical Review A **42** (6), 1990
- [30] A. I. Akhiezer and R. V. Polovin: *Theora of Wave Motion of an Electron Plasma*, Soviet Physics JETP-USSR **3** (5), 1956
- [31] C. M. W. Goedbloed and J. P.: *Magnetically tapered plasma channels for laser wakefield accelerators*, J. Phys. D: Appl. Phys. **41**, 2008
- [32] C. Geddes, K. Nakamura, G. Plateau, E. C.-M. Cs. Toth, E. Esarey, C. Schroeder, J. Cary and W. Leemans: *Plasma density gradient injection of low absolute momentum spread electron bunches*, APS/123-QED 2007
- [33] S. H. Yoo, S. J. Hahn, M. S. Hur, H. Jang, I. Hwang, J. H. K. Suk and Hyyong: *Energy Enhancement of the Self-Modulated Laser Wakefield Acceleration by Using the Plasma Density Gradient*, Journal of the Korean Physical Society 2007
- [34] O. Jäckel: *Characterization of ion acceleration with relativistic laser-plasma*, Friedrich Schiller Universität Jena, Dissertation 2009
- [35] IOQ Jena

## Bibliography

---

- [36] C. Rödel: *Plasmaspiegel zur Kontrastverbesserung von Terawattlaserpulsen für die Erzeugung von Hohen Harmonischen an Oberflächen*, Friedrich Schiller Universität Jena, Diploma thesis 2009
- [37] C. Ziener: *Aufbau eines 12 Terrawatt Titan:Saphir-Lasers zur effizienten Erzeugung charakteristischer Röntgenstrahlung*, Friedrich Schiller Universität Jena, Dissertation 2001
- [38] B.Schmidt, M.Hacker, G.Stobrawa and T.Feurer: *LAB2-A virtual femtosecond laser lab*, <http://www.lab2.de>
- [39] J. Polz: *Zeitaufgelöste Untersuchung der Ionenbeschleunigung bei relativistischen Laser-Plasma-Wechselwirkungen an dünnen Folien*, Friedrich Schiller Universität Jena, Diploma thesis 2008
- [40] F. Budde: *Experiment zur Undulatorstrahlung mit laserbeschleunigten Elektronen*, Friedrich Schiller Universität Jena, Diploma thesis 2007
- [41] A. Buck, K. Zeil, A. Popp, K. Schmid, A. Jochmann, S. D. Kraft, B. Hidding, T. Kudyakov, C. M. S. Sears, L. Veisz, S. Karsch, J. Pawelke, R. Sauerbrey, T. Cowan, F. Krausz and U. Schramm: *Absolute charge calibration of scintillating screens for relativistic electron detection*, Review of Scientific Instruments **81** (3), 2010, times Cited: 6
- [42] I. H. Hutchinson: *Principles of Plasma Diagnostics*, Cambridge University Press 2002
- [43] Idea: [http://www.optics.tugraz.at/idea/Manual\\_IDEA\\_v15.pdf](http://www.optics.tugraz.at/idea/Manual_IDEA_v15.pdf)
- [44] Labview Help
- [45] B. Landgraf: *Charakterisierung von Ueberschalldüsen zur Elektronenbeschleunigung*, Friedrich Schiller Universität Jena, Diploma thesis 2010
- [46] W. P. Leemans, P. Catravas, E. Esarey, C. G. R. Geddes, C. Toth, R. Trines, C. B. Schroeder, B. A. Shadwick, J. van Tilborg and J. Faure: *Electron-Yield Enhancement in a Laser-Wakefield Accelerator Driven by Asymmetric Laser Pulses*, Physical Review Letters **89** (17), 2002

## Bibliography

---

- [47] M. C. Kaluza, H.-P. Schlenvoigt, S. P. D. Mangles, A. G. R. Thomas, A. E. Dangor, H. Schwoerer, W. B. Mori, Z. Najmudin and K. M. Krushelnick: *Title: Measurement of Magnetic-Field Structures in a Laser-Wakefield Accelerator*, Physical review letters 2010
- [48] A. Buck, M. Nicolai, K. Schmid, C. M. S. Sears, A. Savert, J. M. Mikhailova, F. Krausz, M. C. Kaluza and L. Veisz: *Real-time observation of laser-driven electron acceleration*, Nat Phys **advance online publication**, 2011
- [49] T.Feurer: *A Virtual Femtosecond Laser Laboratory*, <http://www.lab2.de>

# Danksagung

Manchmal habe ich mich während meines Studiums gefragt: "Warum mache ich das eigentlich?" Das letzte Mal ging es mir so in dem Semester bevor ich mit meiner Diplomarbeit begonnen habe. Die Arbeit am IOQ und insbesondere mit der JETI-Crew hat mir gezeigt, dass ich wirklich das Richtige gewählt habe.

Viele Menschen standen mir während meiner Diplomarbeit mit Rat und Tat zur Seite. Ich danke euch vielmals für dieses Jahr, welches mich nicht nur fachlich, sondern auch persönlich geprägt hat. Und nun die Liste der VIP:

Ich danke ...

- **Prof. Malte C. Kaluza** für das Thema, welches mich nach wie vor begeistert, die vielen hilfreichen Hinweise und Tipps und natürlich die über das Osterwochenende ausführlich beantworteten Fragen.
- **Alexander Sävert** für die kontinuierliche Unterstützung, die vielen anschaulichen Erklärungen und die Geduld, wenn es mal wieder länger gedauert hat. Ich habe sehr viel gelernt in diesem Jahr.
- **Maria Nicolai**, "die andere Maria" für das Teilen ihres Know-hows rund um Laser-Wakefield Acceleration und das eine oder andere 'Mädchengespräch'.
- **Oliver Jäckel** und **Christian Rödel**, die mir gezeigt haben, wie viel Spaß man im Labor haben kann.
- **Burgard Beleites** und **Falk Ronneberger** für liebevolle JETI-Pflege (auch zu etwas späterer Stunde), und **Wolfgang Ziegler** für das Beachten technischer Details an die sonst keiner denkt.

- **Thomas Barman** für alles rund um Schrittmotoren und die Steuerkisten, sowie allen andern Mitarbeitern der Werkstätten für das schnelle Erledigen vieler Sachen, die auch fast immer gebraucht wurden.
- **Frau Oberheidtmann**, weil sie immer alles mit Humor sieht und für jedes Problem eine Lösung findet.
- **Martin Kahle**, sowie **Jens Polz** und **Diethard Klöpfel** vor bzw. nach meinem Umzug für die angenehme und inspirierende Büroatmosphäre.
- meiner Familie für ihre Unterstützung und den Rückhalt. Meine Mom **Carmen Schneider** hat es einfach drauf, mich aus den schlimmsten Situationen zu retten und mein Vater **Helmut Reuter** fährt auch nachts um drei nach Jena, wenn es mal wieder brennt. Mein Opa **Friedrich Schneider** hat mir meine Zeit in Schottland unheimlich erleichtert.
- **Claudi & Kalki, Oli & Caro, Marcus, Christian & Donna**: Danke für eure Zeit, euer Verständnis und weil ich mich einfach so gern habt, wie ich bin

achja genau

- **meinen Jungs vom IAO** weil sie extra für mich ihre heilige Mittagszeit von 11 auf 13 Uhr verlegt (und mich nur selten vergessen 😊 ) haben



# Erklärung

Hiermit erkläre ich, dass ich die vorliegende Arbeit selbstständig verfasst und keine anderen als die angegebenen Quellen und Hilfsmittel genutzt habe. Seitens des Verfassers bestehen keine Einwände, die vorliegende Diplomarbeit für die öffentliche Nutzung in der Thüringer Universitäts- und Landesbibliothek zur Verfügung zu stellen.

Jena, den